Department of Physics and Astronomy
University of Heidelberg

Bachelor Thesis in Physics
submitted by

Jonas M. Mikhaeil

born in Mönchengladbach (Germany)

2019

Topological Shower Reconstruction in a Highly Granular Calorimeter with Optical Readout

This Bachelor Thesis has been carried out by Jonas M. Mikhaeil at
DESY in Hamburg
under the supervision of
PD Dr. Felix Sefkow

Abstract

The CALICE AHCAL engineering prototype is a highly granular particle flow calorimeter with optical readout. As such it offers the possibility to reconstruct topological shower information. In this work an algorithm based on the sharp rise in layer-wise measured energy after the first hadronic interaction was implemented and optimized to extract the shower start. This high-level shower variable was used to measure the pion interaction length $\lambda_\pi = 27.94 \pm 0.15(\text{stat}) \pm 0.48(\text{sys})$ cm of the detector. The measured value is in excellent agreement with the value $\lambda_\pi = 27.76$ cm obtained from the material composition of the detector. As particle flow calorimeters are spatially constraint, shower leakage is an issue. Topological shower information can be used to correct this leakage . In this work a correction for longitudinal shower leakage is implemented on the basis of the shower start and the end-fraction, the fraction of the shower energy in the last four layers of the detector. The leakage correction was found to improve the simulated energy resolution by up to 41%. A preliminary study of the application of the implemented leakage correction on data was performed, yielding an energy resolution improved by up to 33%.

Abstract

Der CALICE AHCAL technologischer Prototyp ist ein hoch granuläres Particle Flow Kalorimeter mit optischer Auslese. Als solches ermöglicht es die Rekonstruktion von topologischer Information von Teilchenschauern. In dieser Arbeit wurde ein Algorithmus, basierend auf der starken Zunahme der gemessenen Energie in den Lagen nach der ersten hadronischen Wechselwirkung, implementiert und optimiert, um den Start eines Teilchenschauers zu extrahieren. Diese Schauervariable ermöglicht die Messung der Pionen Interaktionslänge $\lambda_\pi = 27.94 \pm 0.15(\text{stat}) \pm 0.48(\text{sys})$ cm des Detektors. Der gemessene Wert stimmt exzellent mit dem Wert $\lambda_\pi = 27.76$ cm basierend auf der Materialzusammensetzung des Detektors überein. Da Particle Flow Kalorimeter räumlichen Einschränkungen unterliegen, ist das Austreten von Schauerteilchen aus dem Detektor ein Problem. Topologische Schauerinformationen können genutzt werden, um die Messung zu korrigieren. In dieser Arbeit wurde eine Korrektur des longitudinalen Schaueraustritts auf der Basis des Schauerstarts und des End-Anteils, des Anteils der Schauerenergie in den letzten vier Lagen des Detektors, implementiert. Diese Korrektur verbessert die simulierte Energieauflösung um bis zu 41%. Es wurde eine vorläufige Studie zur Anwendung dieser Korrektur auf Daten durchgeführt, welche eine um 33% verbesserte Energieauflösung zeigte.

Contents

Introduction

Particle physics strives to discover and understand the fundamental building blocks of Nature, *elementary particles*, and the interactions between them, the *fundamental forces*. Decades of research culminated in the *Standard Model* (SM) of particle physics, which is able to successfully describe all current experimental data. It describes Nature in terms of six quarks and leptons and five gauge bosons, as depicted in Figure 1. Its final piece, the Higgs boson, was discovered by the ATLAS and CMS experiments at the Large Hadron Collider (LHC) in 2012 [1] .

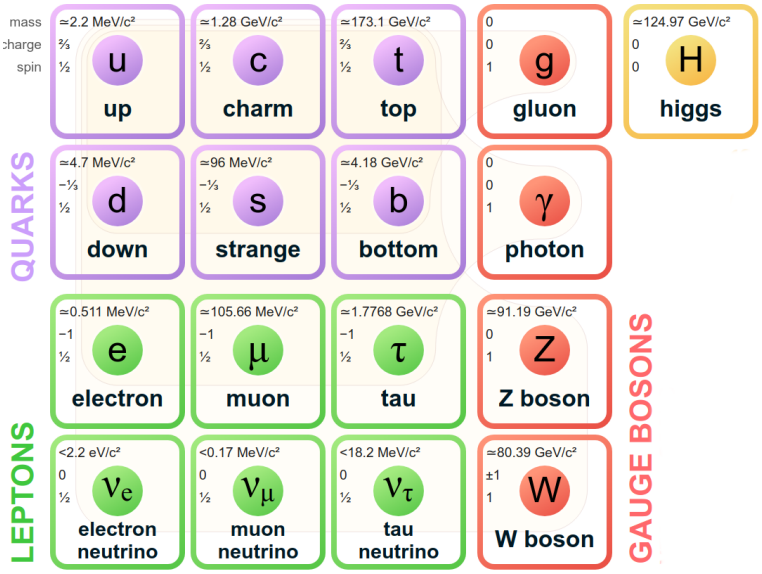

Figure 1: The elementary particles of the Standard Model. 12 fundamental fermions, constituted by six quarks and six leptons, and 4 fundamental gauge bosons. 2012 the Higgs boson was added. Beige loops illustrate which gauge bosons couple to which fermions. The Higgs boson couples to all massive particles [5].

To investigate the properties of the Higgs boson with satisfactory precision, future particle physics projects will have to reconstruct the beam interaction final states with increasing detail. Because of the mass of the Higgs $m_H = 125.18 \pm 0.16$ GeV [2], the next generation of e^+e^- colliders, like the *International Linear Collider* (ILC), aim for centre-of-mass energies of 250 GeV or above. These energies lead to extensive production of W- and Z -bosons. These have to be reconstructed in multi-jet final states and be distinguished by their invariant mass. If a 3σ separation is to be achieved, taking into account the W - Z mass separation of 10 GeV and the natural width of their mass distribution of roughly 2.7%, an unprecedented jet-energy resolution of 3-4% over a wide range of jet-energies is required [3].

Classically in a collider detector, jet energies are measured by summing up all energy depositions of charged and neutral jet particles in the calorimeter system, which surrounds a tracker system for the detection of charged particles. For reasons expanded on later (See Section 1.2.1) this approach is unlikely to achieve the jet-energy resolution goal of 3-4%. To accomplish the necessary resolution the particle flow (PFlow) approach was developed. The PFlow method aims to optimize the jet-energy resolution by reconstructing each jet particle individually to then use the energy measurement of the best suited sub-detector for the particle type in question [4]. The central aspect of Pflow calorimetry is thus the matching of the energy depositions with the correct particles. This is a complex pattern recognition problem, which requires a highly granular calorimeter system to include topological information [3].
This topological shower information allows a novel way of studying showers in the calorimeter. In this thesis we will use topological information to reconstruct the shower starting point. This will allow us to determine the pion interaction length of the detector under study and to implement a correction for longitudinal shower leakage.
The first chapter introduces particle flow calorimeters in the context of the International Large Detector. The basic processes in calorimeters are briefly covered and the particle flow approach is motivated by the limitations of classical calorimetry.
The second chapter covers the CALICE engineering prototype, one such particle flow calorimeter, its calibration, particle shower simulations and event selection.
The implementation and optimization of a shower start finder is discussed in chapter three.
One the basis of this algorithm, the pion interaction length of the CALICE engineering prototype is determined in chapter four and used as a cross-check for the value obtained from the material composition of the detector.
The final chapter covers the implementation of a longitudinal leakage correction on the basis of topological shower information for the CALICE engineering prototype. The impact of the correction is studied for simulations and testbeam data.

1 Particle Flow Calorimeter

Even though tracking is an essential part of the Particle Flow approach, we will, due to the scope and focus of this thesis, only spotlight the most important process in the calorimeter system.

1.1 Basic Processes in Calorimeters

There is an abundance of elementary and composite particles, the *particle zoo*, that can be created in particle collisions. Most of them decay into more stable particles before reaching the calorimeter. Thus instead of having to deal with an entire zoo, the list of particles we have to deal with in by far the most cases, consists only of: $e^{\pm}, \mu^{\pm}, \gamma, \pi^{\pm}, K^{\pm}, K^0, p^{\pm}, n, \nu$. Broadly, these can be categorized two-fold. Firstly only the charged particles generate a signal in the tracker, whereas the neutral particles typically do not. A further distinction can be drawn by the fact that $e^{\pm}$ and γ induce electromagnetic showers in contrast to $\pi^{\pm}, K^{\pm}, K^0, p^{\pm}, n$, which create hadronic showers. Muons typically only leave a minimally ionizing track behind. The most eery particle is the neutrino, almost never interacting with matter and thus traversing the calorimeter without generating any signal - invisibly carrying away momentum [6].

1.1.1 Electromagnetic Cascades

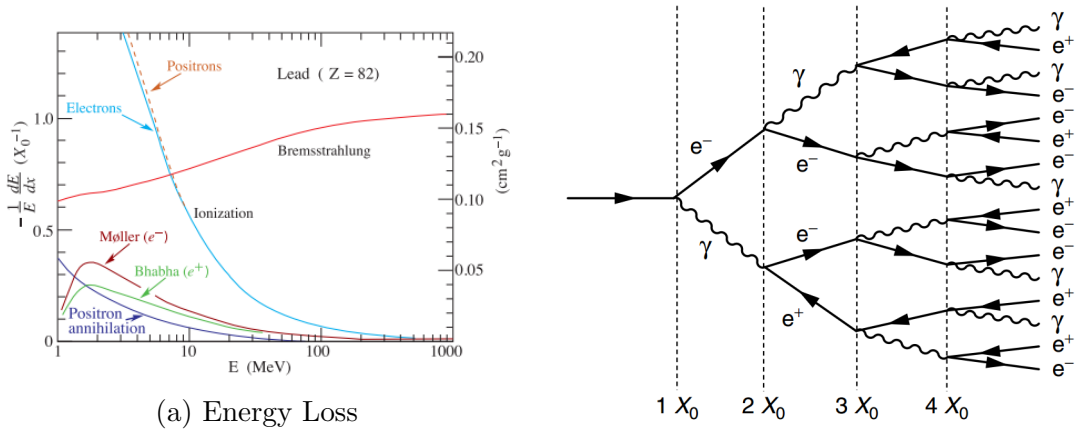

(a) Energy Loss

(b) Electromagnetic Cascade

Figure 2: Fractional energy loss per radiation length in lead as a function of electron or positron energy [2] and simplified picture of an electromagnetic cascade [1].

As Figure 2 (a) indicates, electrons above a *critical energy* ϵ_c passing through matter loose their energy mainly due to *Bremsstrahlung* - which is radiation

produced by the change in momentum of charged particles. Electrons in matter interact with the Coulomb field of nuclei and emit a photon due to the resulting acceleration. The energy E of the emitted photons follows an $\frac{1}{E}$ dependence. Typically only a small fraction of the electron's initial energy is radiated per interaction [7]. The energy loss per unit length, dE/dX, of an electron due to this process is roughly proportional to its energy

$$-\left[\frac{dE}{dX}\right]_{Brems} = \frac{E}{X_0} \tag{1}$$

with X_0 being the *radiation length* [6]. The value of X_0 is material dependent - a common parametrization depending on the atomic number Z and the mass number A is given in [2] as

$$X_0 = \frac{716.4A}{Z(Z+1)\ln(287/\sqrt{Z})} g\ cm^{-2}. \tag{2}$$

High energy photons - for example radiated due to Bremsstrahlung - traversing matter can undergo electron-positron pair production if their energy is above the production threshold $E_\gamma \geq 2m_e \approx 1\text{MeV}$, where m_e is the mass of the electron. The mean free path length of these photons before pair production is given by $\frac{9}{7}X_0$ [7].
In this way a high energy electron or photon entering a dense material sets off an electromagnetic cascade by a combination of Bremsstrahlung and pair production. As Figure 2 (b) shows, the number of particles in such an *electromagnetic shower* roughly doubles for every X_0 of traversed matter. Individual branches of the shower die off when the energy of the involved electron drops below ϵ_c, where the energy loss is dominated by ionization. This critical energy is material dependant and can for solids be parametrized as [7]

$$\epsilon_c = \frac{610\ \text{MeV}}{Z + 1.24} \tag{3}$$

1.1.2 Heavy Charged Particles

Charged hadrons and muons loose their energy mainly due to ionization, because Bremsstrahlung is suppressed by the particle's mass m as

$$\left[\frac{dE}{dX}\right]_{Brems} \propto \frac{1}{m^4} \tag{4}$$

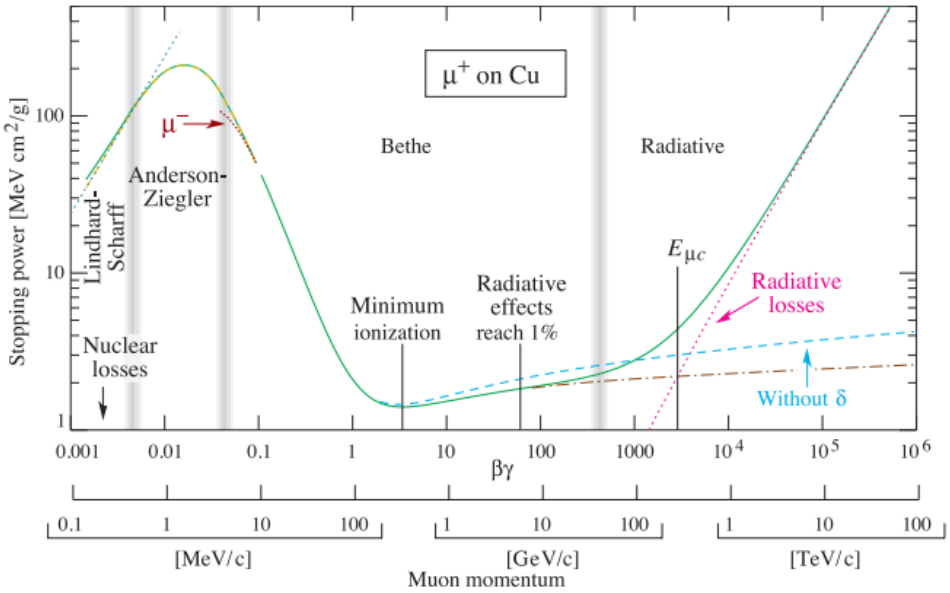

Figure 3: Stopping power ($=\langle -dE/dx \rangle$) for positive muons in copper as a function of $\beta\gamma = p/Mc$. Solid curves illustrate total stopping power [2].

The mean energy loss of these heavy charged particles as a function of their velocity $v = \beta c$ (c is the speed of light) is given by the Bethe equation [2] as

$$-\left\langle \frac{dE}{dx} \right\rangle = Kz^2 \frac{Z}{A} \frac{1}{\beta^2} \left[\frac{1}{2} \ln \frac{2m_e^2 \beta^2 \gamma^2 T_{max}}{I^2} - \beta^2 - \frac{\delta}{2} \right] \tag{5}$$

in which K is a proportionality constant, T_{max} the maximal kinetic energy that can be passed on to an electron in one collision and I is the mean excitation energy of the absorber material. δ corrects for the density effect [7].
Figure 3 shows the mean specific energy loss for positively charged muons in copper. Around $\beta\gamma \approx 4$ a wide minimum, the *minimum ionizing particle* (MIP) region, is clearly visible. The distribution of the energy deposition of charged particles in layers of "moderate thickness" follows a Landau distribution, as depicted in Figure 4 [2].

1.1.3 Hadronic Cascades

Besides ionization, charged hadrons also interact strongly - via the strong force - with the nuclei of dense matter. Inelastic *hadronic interactions* can lead to a variety of nuclear reactions, including spallation, fission and nuclear breakup, typically creating secondary mesons ($\pi^{\pm}, \pi^0, \eta, ...$) and ejection of protons and neutrons from the nucleus. The number, composition and momenta of these secondary particles can fluctuate strongly; secondary hadrons of sufficient energy

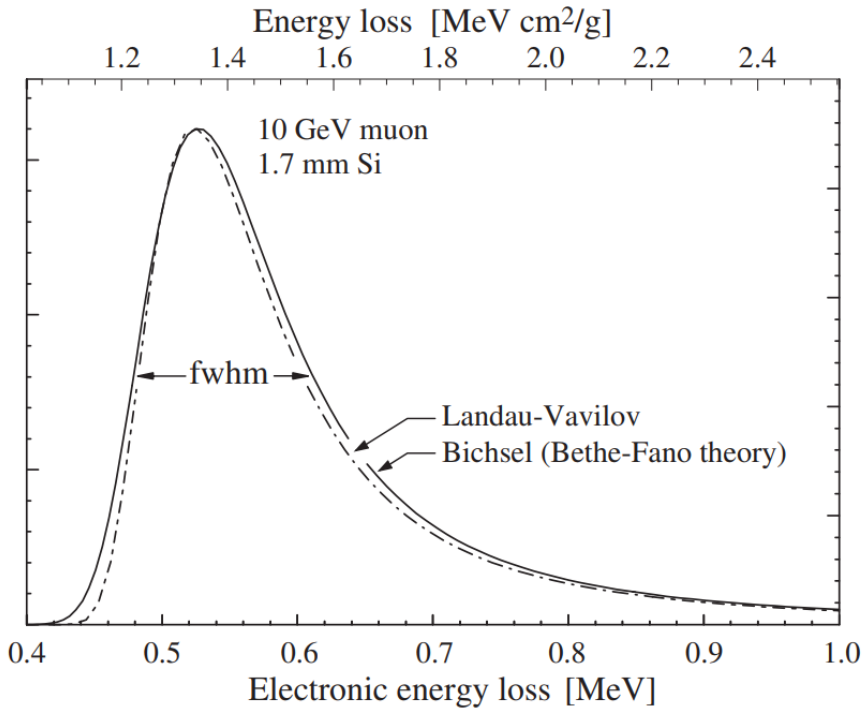

Figure 4: Distribution of the energy deposition of a 10 GeV muon in a 1.7 mm Si layer [6].

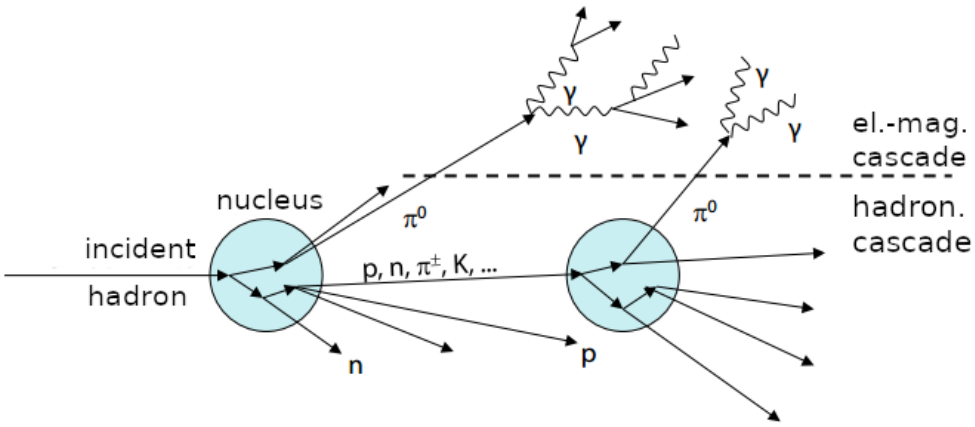

Figure 5: Simplified depiction of a hadronic shower. Adapted from [12].

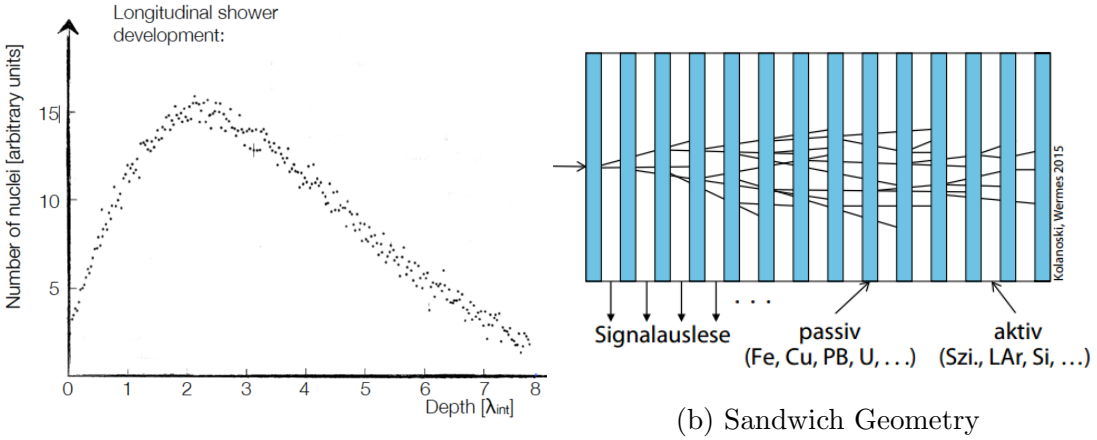

(a) Longitudinal shower profile

(b) Sandwich Geometry

Figure 6: Longitudinal shower profile for 300 GeV π^- in a block of uranium [7] and schematic depiction of a sampling calorimeter with sandwich geometry [12].

can undergo hadronic interactions themselves, kicking off a *hadronic shower*. Secondary π^0 and η decay into photons, creating an electromagnetic sub-shower [6]. The energy fraction contained in these electromagnetic sub-showers fluctuates strongly from event to event. On average, approximately one-third of the produced mesons will decay electromagnetically, increasing slightly with energy [7]. Due to recoil or excitation of the struck nucleus on average 20% of the energy transferred to the nucleus is *invisible*. The *nuclear interaction length* λ_n is the mean free path between such hadronic interactions. For materials with $A > 7$, λ_n can be parameterized [10] as

$$\lambda_n = \left(20A^{0.4} + 32\right) g\ cm^{-2} \tag{6}$$

The *pion interaction length* λ_π is typically elongated by a factor of $\frac{3}{2}$ compared to λ_n. Compared to purely electromagnetic showers, hadronic showers are typically much larger in extension due to $\frac{\lambda_n}{X_0} \gg 1$. Because hadronic showers are created by only a few hard hadronic interactions, which vary considerably in the number of secondary particles produced, they are characterized by large statistical fluctuations in extensions, as well as the energy fraction, which is invisible or contained in electromagnetic sub-showers [6].

1.2 Classical Calorimetry and its Limitations

In high energy physics, calorimeters measure the energy of particles by full absorption and subsequent measurement of the deposited energy. This approach is only possible due to the fact that shower size scales merely *logarithmically* with

energy. Moreover, dense absorber material is used to restrain the total shower size.

Homogeneous calorimeters consist of absorber material that is itself producing a signal corresponding to the energy deposited. Because of spacial constraints high density scintillating crystals such as $PbWO_4$ ($\rho = 8.2\ g\ cm^{-3}$) are used [11].

Sampling calorimeters on the other hand interlace dense but passive absorber material with sensitive detector layers. This allows to choose the optimal absorber and active material depending on the requirements of the experiment, separately. Because most of the energy is deposited in the absorber material and thus not measured, the energy in the active layers has to be extrapolated to the entire shower energy. Of particular interest for us are *sandwich* calorimeters, see Figure 6 (b) , in which layers of absorber and active material are alternated - establishing granularity along the longitudinal shower axis [6].

Due to fluctuations in the fraction of energy deposited in the active material, the energy resolution of sampling calorimeters is degraded compared to homogeneous ones.

Another factor that reduces the energy resolution of hadronic calorimeters is *non-compensation* - the different detector response to hadronic and electromagnetic showers of the same energy. This is due to the fraction of invisible energy in hadronic showers. This $\frac{e}{h}$ ratio is larger than unity in most calorimeters and can even increase beyond the fraction of invisible energy from inefficiencies in detecting neutrons from hadronic interactions. Because of the sizable fluctuations in the energy fraction of the electromagnetic sub-showers of hadronic cascades, a $\frac{e}{h} \neq 1$ leads to a degradation of the energy resolution [6].

1.2.1 Energy Resolution

The afore-mentioned energy resolution is the most important measure of merit for a calorimeter. In most calorimeters the energy resolution is limited by stochastic fluctuations of the number of charged shower particles. Their number N_s is proportional to the primary energy of the incident particle, $N_s \propto E$. Counting processes like this one are described by a Poisson probability distribution; N_s thus has a standard deviation of $\sqrt{N_s}$. For the energy resolution consequentially

$$\frac{\sigma_E}{E} \propto \frac{\sqrt{N_s}}{N_s} = \frac{1}{\sqrt{N_s}} \propto \frac{1}{\sqrt{E}} \tag{7}$$

holds. As illustrated above, there are other effects with various energy dependence contributing to the energy resolution as well. An ansatz to describe the energy

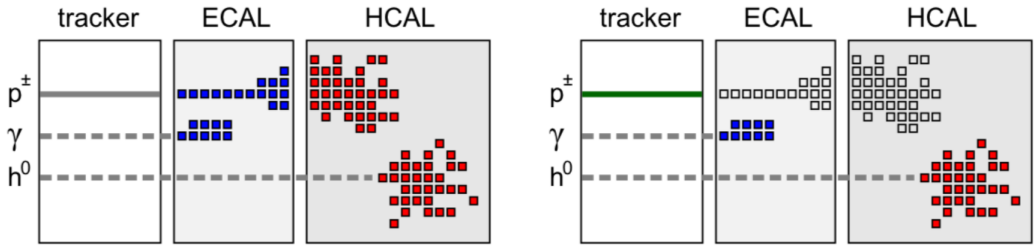

Figure 7: Comparison of classical and PFlow jet energy reconstruction [6].

resolution more universally is given by

$$\frac{\sigma_E}{E} = \sqrt{\frac{a^2}{E} + \frac{b^2}{E^2} + c^2} := \frac{a}{\sqrt{E}} \oplus \frac{b}{E} \oplus c \qquad \text{with } E \text{ in GeV} \tag{8}$$

Major contributions to the different terms are given by

a the afore-mentioned statistical fluctuations in shower development,

b electronic noise, which contributes to the relative energy resolution with $1/E$ because of its absolute energy independence [12],

c detector inhomogeneities [6], as well as the degree of non-compensation $|e/h - 1|$ [7]

As described in the introduction (See Section), we are interested in the jet-energy resolution of calorimeter systems. As an example of a currently operating hadronic calorimeter, the ATLAS hadronic tile calorimeter yields a single hadron energy resolution best described by $a = 52.9\%$ and $c = 5.7\%$ under testbeam conditions [6]. This is typical for classical calorimeter systems: The stochastic terms a ranges from $50 - 100\%$, with c being in the order of a few percent [4]. Because particle jets created in high energy processes carry large fractions of their energy in hadrons, it is unlikely that classical calorimetry is able to achieve the goal of 3-4% jet-energy resolution for jet-energies below a few hundered GeV [3].

1.3 The Particle Flow approach

The particle flow approach is a modern concept made possible by the progress of tracking detectors and highly granular calorimeters in the last two decades. Key to this idea is that up to very high single particle energies - around 500 GeV in the HCAL - the tracking resolution for charged hadrons is superior to the calorimeter resolution.

Thus instead of discarding the tracking information for charged hadrons, as the

classical approach does, *Particle Flow Algorithms* (PFAs) aim to reconstruct each jet particle individually to then use the measurement of the best suited sub-detector. Accordingly, the energy of charged particles is determined in the tracker and photons are captured by the ECAL. Only neutral hadrons are measured by the combined ECAL and HCAL system, avoiding the HCAL's limiting energy resolution for every other particle type.
Considering that on average only 10% of jet particles are neutral hadrons, 27% are photons and approximately 60% are charged particles, the particle flow approach can drastically improve the energy resolution. Assuming a calorimeter resolution of $\sigma_E/E = 0.15/\sqrt{E}$ for photons and $\sigma_E/E = 0.55/\sqrt{E}$ for neutral hadrons, a jet energy resolution of $0.19/\sqrt{E}$ would be obtained. In practice this level of performance is not entirely achievable, because it is not possible to associate every energy deposition with the correct particle [3].
The particle flow approach includes the superior tracking resolution for charged particles by introducing a complicated pattern recognition problem. To make this problem tractable, topological shower information within the calorimeter system is needed. The particle flow approach therefore creates novel challenges in detector development.

1.4 The International Large Detector

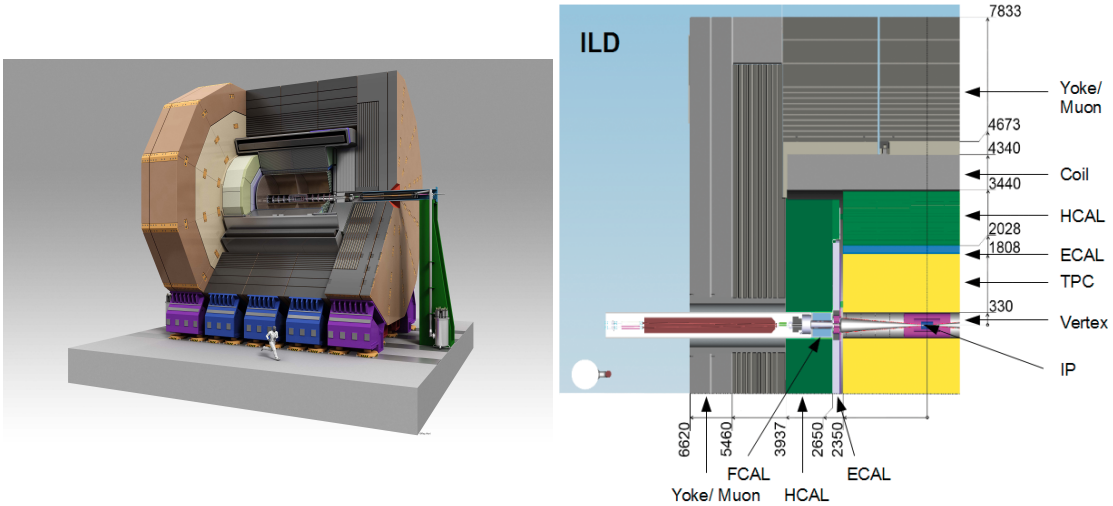

Figure 8: ILD detector and quadrant view [13].

One multi-purpose detector design developed to rise to these challenges is the *International Large Detector* (ILD).
As Figure 8 illustrates, the ILD is planned to be constructed in a close to cylindrical shape with a length of 13 m and a radius of 7.8 m. To allow matching of

tracks and showers in the calorimeter system, both the tracking system as well as the calorimeters are located inside the superconducting solenoid coil of 3.4 m inner radius. This magnet will create a field of 3.5 T oriented in parallel to the beam axis [13].

A distinct feature of the ILD and an essential part of the tracking system is a large volume *Time Projection Chamber* (TPC) with up to 224 points per track. Charged particles ionize the gas inside the TPC resulting in free electrons. These are accelerated towards the endcaps by an electric field, where they are detected by a gas electron multiplier or micro-mesh gaseous structure. Additionally, measurements of the ionization strength allow particle identification based on the deposited energy density dE/dx. The complete tracking system has a design momentum resolution of $\sigma_{1/p_T} \approx 2 \cdot 10^{-5}$ GeV^{-1} [13].

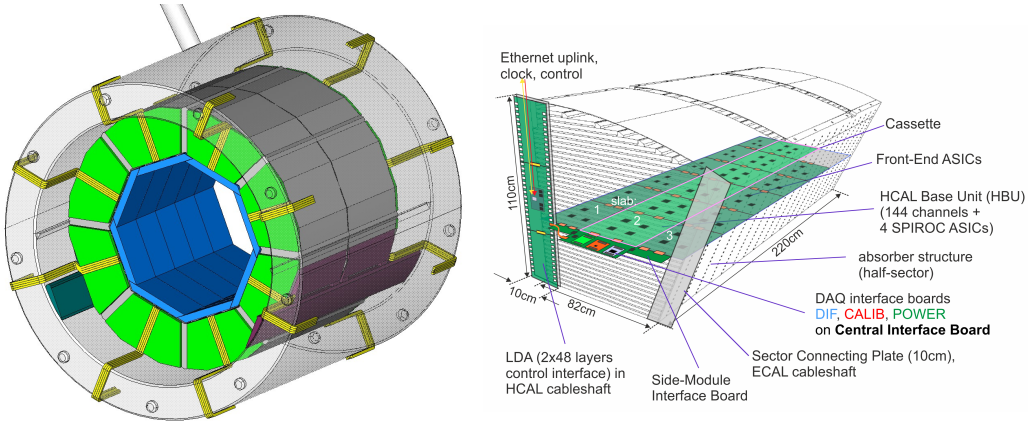

Figure 9: Sketches of the ILD AHCAL [6].

The HCAL is designed to be highly granular with 40 to 48 active layers interleaved with 20 mm steel absorbers. The *Analogue Hadron Calorimeter* (AHCAL) option uses 3×3 cm^2 scintillator tiles which are read out individually by *silicon photomultipliers* (SiPMs) to gather transverse spatial information. In total it is anticipated to have eight to ten million individual cells. Due to this high channel density all signal digitization as well as the readout electronics have to be fully integrated into the active layers. Moreover, in order to fit the AHCAL into the solenoid coil the thickness of the active layers has to be minimal. For this reason no active cooling is feasible, limiting the power dissipation of the readout electronics to 25 μW per readout channel [6]. The engineering design for the hadronic calorimeter of the ILD is sketched in Figure 9.

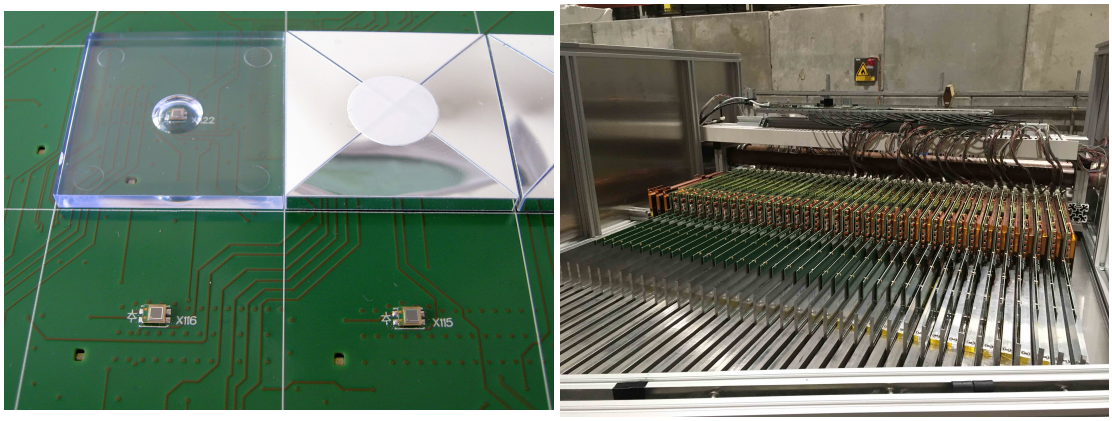

(a) Scintillator tiles and SiPMs

(b) AHCAL engineering prototype

Figure 10: Scintillator tiles with central dimple mounted on an HBU with the visible SiPMs: Wrapped and unwrapped for comparison. These are employed in the AHCAL engineering prototype setup for testbeam measurements [14].

2 The CALICE Analogue Hadron Calorimeter

After comprehensive tests with beams at DESY, CERN and Fermilab, the physical performance properties of the ILD AHCAL concept were demonstrated by the CALICE collaboration with a cubic-metre sized AHCAL physics prototype. Having established the principle validity of the technology, the focus of the current CALICE AHCAL engineering prototype is to establish the feasibility of the detector concept under spatial constraints and scalability requirements [14].

2.1 The CALICE SiPM-on-Tile Hadron Calorimeter Engineering Prototype

The CALICE AHCAL engineering prototype is made up of non-magnetic stainless steel absorber, that allows operation in a strong magnetic field. It consists of 38 active layers and a total number of 21888 channels, ensuring longitudinal as well as lateral granularity. The active layers are comprised of *HCAL Base Units* HBUs, each having a size of 36×36 cm^2 and carrying 144 SiPMs. These are read out via four SPIROC2E ASICs per HBU. As shown in Figure 10 (a), the prototype is equipped with Hamamatsu MPPC S13360-1325PE photon sensors within injection-moulded polystyrene scintillator tiles with a central dimple to allow for uniform light collection. As discussed in Section 1.4, the detector design necessitates low power consumption of the readout electronics. This is achieved by rapidly cycling the power so that the analogue part of the electronics is powered off during data transfer, *power pulsing*, also eliminating the need for

material	integrated λ_π	d_{layer}[cm]	d_{total}[cm]	λ_π[cm]
Steel plate	3.195	1.72	65.36	20.46
Casette plates	2×0.093	2×0.05	2×1.9	20.46
Scintillator tile	0.106	0.3	11.4	107.2
Foil	2×0.0003	2×0.011	2×0.418	107.2
Cable	0.061	0.15	5.7	91.9
PCB	0.036	0.07	2.66	74.02
Air		0.257	9.766	
AHCAL	3.585		99.522	27.76

Table 1: Material composition of the AHCAL engineering prototype. The pion interaction length for each material was calculated on the basis of its atomic composition and information from [2]. Information concerning the cable mix are taken from [17].

active cooling [14].

The prototype has been assembled with techniques suited for mass production. These include injection-moulding and semi-automatic wrapping of the scintillator tiles, the assembly of scintillators on electronics using pick-and-place machines as well as mass testing of detector elements.

Figure 10 (b) shows the active layers placed into the absorber stack and connected to data concentration, power distribution and cooling services. This setup was installed at the CERN SPS during two periods in May and in June 2018 to take several 10^7 events with muon tracks, as well as electron and pion showers [14]. The high granularity of the AHCAL engineering prototype allows to determine the first hadronic interaction layer and thus a measurement of the pion interaction length. This can serve as a cross-check of the material composition of the detector. λ_π is given by the length of the detector divided by the integrated interaction length of the 38 detector layers - including both the active material, as well as the corresponding steel plate. Any additional detector material up- or downstream of these layers can be neglected, as it is not captured by our later analysis and is thus not part of the cross-check. Table 1 shows the interaction length for each contributing material. These values are obtained on the basis of the materials atomic composition and information from [2]. The interaction length of the cable mix is adapted from [17].

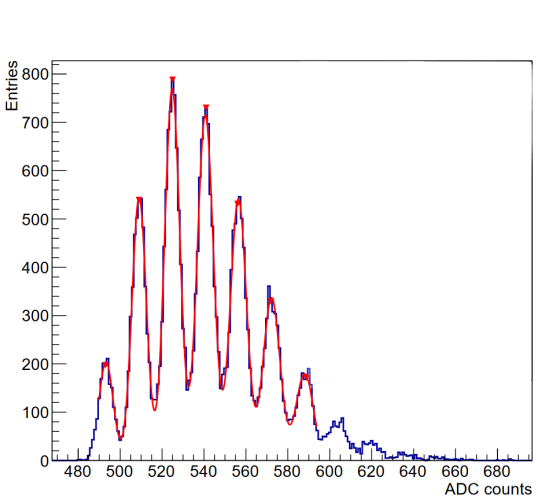

(a) Single photo-electron spectrum

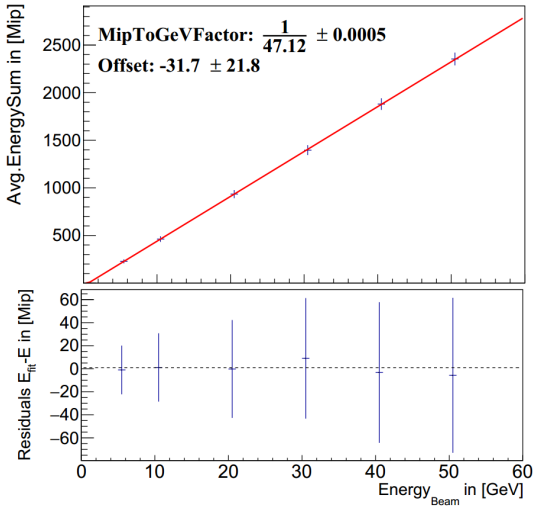

(b) Response to electrons vs. beam energy and electromagnetic scale factor

Figure 11: (a) Single photo-electron spectrum: The pedestal can be extracted as position of the first peak. The gain corresponds to the difference of consecutive peaks. Adapted from [15]. (b) The electromagnetic scale factor is determined by fitting the energy response of the entire detector to electrons as a function of the beam energy.

The CALICE AHCAL engineering prototype is found to have an overall integrated pion interaction depth of 3.6 lambda, yielding an averaged pion interaction length of $\lambda_\pi = 27.76$ cm.

2.2 Calibration

To extract a meaningful energy measurement, the detector response has to be calibrated. This is achieved with

$$E_{calibrated}[\text{MIP}] = f_{desat}(\text{pixel})\frac{(ADC - \text{Pedestal})/IC}{mip} \tag{9}$$

a channel-wise calibration: First, the pedestal - the electronic-base line corresponding to no signal- is subtracted from the digitized but uncalibrated energy measure ADC, see Figure 11 (a). This value is adjusted with an *intercalibration factor* IC taking care of the different gains corresponding to two modes of amplification for different signal strengths. For high energy depositions, the number of fired $pixel = \frac{(ADC-\text{Pedestal})/IC}{Gain}$ is in the order of the effective number of pixel of the SiPM. $f_{desat}(\text{pixel})$ corrects for the ensuing saturation effects, which are due to the finite total number of pixels and their final recovery time. To equalize the

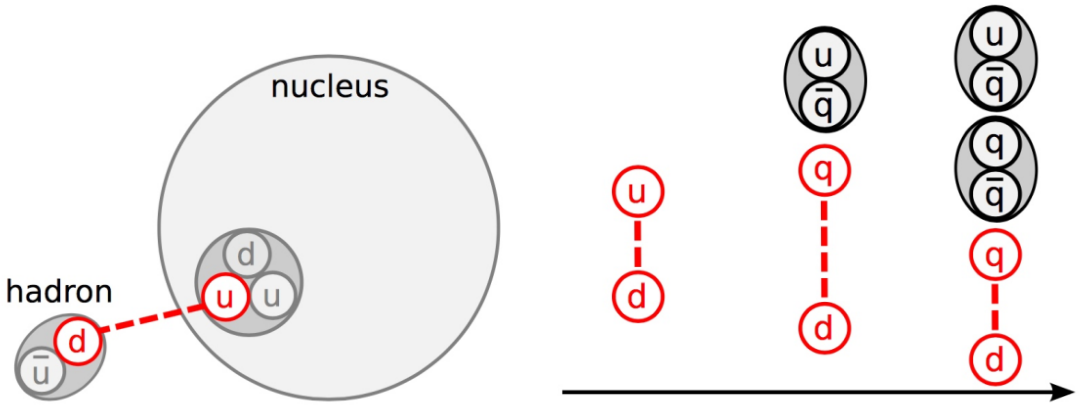

(a) String Formation

(b) String Fragmentation

Figure 12: Formation of a gluon string between the projectile and one of the quarks inside the nucleus and gluon string fragmentation via the generation of quark-antiquark pairs and their subsequent hadronisation [11].

output of all channels, the result is scaled to the most probable energy deposition of a minimum ionizing particle *mip* (see Section 1.1.2). These calibration constants (Pedestal, *mip*) have to be determined individually for the 16 memory cells for each of the 21888 channels of the detector. [15]
There are various ways to connect these calibrated values with a physical energy scale. In this thesis, we used simulated electrons to determine the *electromagnetic scale factor a*. As seen in Figure 11, this is done by comparing the integrated energy of the entire detector in units of MIP with the energy of the incident electron in GeV. Fitting the energy response to the energy of the incident particle, an offset has to be allowed to take care of noise and threshold effects [6].
The scale factor and the offset are determined to be $a = \frac{1}{47.12} \pm 0.0005 \ \frac{\text{GeV}}{\text{MIP}}$ and $b = -37.7 \pm 21.8$ MIP, respectively.

2.3 Simulation of Particle Showers

GEANT4 [8] is a widely used toolkit to simulate particle interactions with matter in a wide range of energies.
Electromagnetic cascades are generally well understood due to their simple interactions. They are simulated with a standard EM package within GEANT4, reproducing observables in sampling calorimeters to a level of $< 1\%$.
Hadronic showers are more complex due to the compositeness of both the projectile hadron and the target nuclei. Up to now, there is no model of hadron cascade development reaching the same accuracy for hadronic shower observables, as what has been established for electromagnetic showers. However, significant progress

has been made in recent years with considerable help from the CALICE collaboration [14].
For energies up to a few GeV, the de Broglie wavelength of the projectile λ is in the order of the distance between nucleons but larger than the quark substructure. In this case, the interaction can be described by *intra-nuclear cascade* models. The GEANT4 model used for the simulations in this work is the Bertini cascade model, in which the nucleus is modelled as three spherical shells of constant nucleon density. Nucleons in each shell are treated as a Fermi gas, occupying all energy states up to the Fermi energy. The intra-nuclear cascade concludes when the projectile hadron and all generated secondary particles are either absorbed in or have left the nucleus [6].
In the energy regime of > 5 GeV, parton string models are applied. The projectile is assumed to initially interact with only a single target nucleon of random momentum up to the Fermi momentum. As Figure 12 sketches, a gluon string is generated between one quark of the projectile and the target nucleon each, which fragments within the nucleus. This causes excitation of the nucleus and the generation of secondary particles. The GEANT4 *quark-gluon string* model is used for the simulations in this work.
A phenomenological parametrization is used to fill the gap in energy coverage of the Bertini cascade model and the *quark-gluon string* model [6].
The output of these GEANT4 simulations consists of energy depositions in the volumes marked as active material in the simulation geometry. As the raw output of the detector consists of digitized measured voltages in hardware units (ADC), it is necessary to transform the raw simulation output into a structure resembling the raw data format. To obtain realistic results this *digitization* has to include an appropriate modeling of readout effects arising from the combination of the used active material as well as the sensors and electronics. These include binomial smearing of the channel amplitudes due to finite number of SiPM pixels and trigger threshold effects. After *digitization* simulated events can be reconstructed with the same software chain used for raw data [6].

2.4 Event Selection

To perform analysis of the data taken at the CERN SPS focused on a single particle type, a proper event selection is required. Particles of various types and energies are created at the SPS as a secondary beam produced by target collisions of a high energy (up to 400 GeV) primary proton beam. This secondary beam is filtered by collimators and magnets to provide the testbeam of requested particle

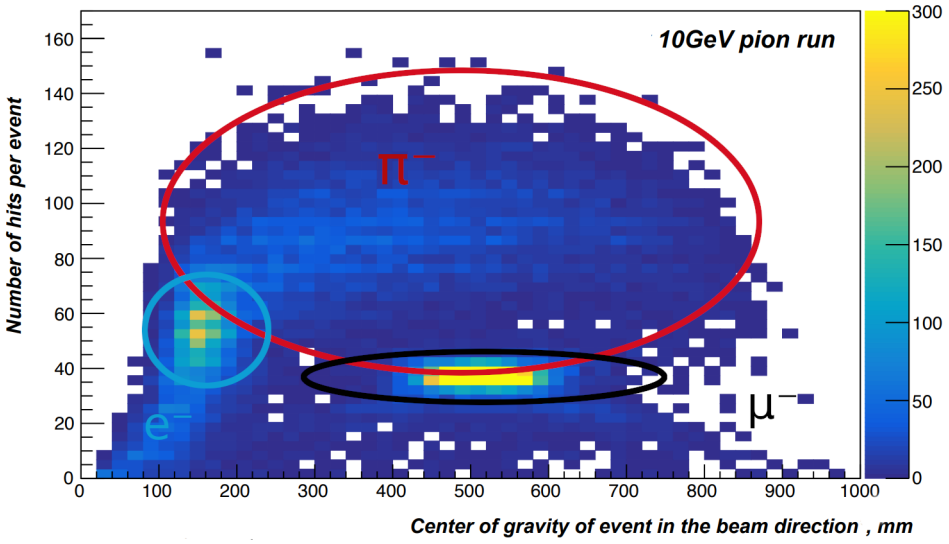

Figure 13: Correlation plot of energy-weighted center-of-gravity against number of hits for a run with electrons, muons and pions. Adapted from [18].

type and energy.

Muons are obtained from a collimated pion beam which is stopped before the last bending magnet, electrons are produced via gamma conversion by directing a photon beam at a lead target. For a pion beam, the momentum is selected by a set of collimators and magnets. Due to π^0 decays and subsequent photon conversion in the absorber filter, an electron contamination of low momentum pion beams (< 20 GeV) is possible [11].

Testbeam data is thus susceptible to varying degrees of contamination, making event selection for samples of insufficient purity necessary. Figure 13 shows the correlation of the energy-weighted centre-of-gravity

$$z_{CoG} = \frac{\sum_{i=1}^{N_{hits}} z_i E_i}{E_{sum}} \tag{10}$$

and the number of hits for a 10 GeV run containing electrons, muons and pions. Electrons and muons are well separated; for effective pion identification, classification in a higher dimensional space is advantageous. As detailed in [18], cuts in five dimensions are applied to classify events. Table 2 specifies these cuts: if an event is not classified as an electron, the cuts for a muon-like event are checked. Events classified as being neither electrons or muon-like are categorized as hadrons.

Performance tests of this event selection employing simulated events for which the particle type is known, show the misidentification probability for hadron classification (e.g. the fraction of particles wrongly identified as hadrons) to be 0.3%

Cut	Electron Events	Muon-like events
		not classified as electron
Hits:	$45 < n_{hits} < 95$	$0 < n_{hits} < 70$
Shower start layer:	st<10	
Shower radius:	0 <r <65 [mm]	$0 < r < 30$ [mm]
Centre of gravity:	$z_{CoG} < 400$ [mm]	$260 < z_{CoG} < 800$ [mm]
Fraction in first 25 layers:	fr_{25} >90%	fr_{25} <95%

Table 2: Cuts to identify electron and muon-like events. If an event is classified to be neither an electron nor muon-like, it is classified to be a hadron [18].

for both electrons and muons [18].
Some of these cuts are energy-dependent and have to be tuned for every relevant energy to achieve optimal performance. For later analysis in this work, the optimal cuts for 30 GeV pions were determined. To exclude electron contamination at higher energies, the hits cut was adapted to be $45 < n_{hits} < 180$ - allowing to filter high, as well as low energy electrons. The muon-like cuts do not change as the detector response to these events is practically energy independent. These cuts yield a hadronic misidentification probability of 1.2% and 0.5% for muons and electrons, respectively. The efficiency of the event selection (e.g. the probability to identify a hadron as such) for both energies is found to be roughly 94%.

3 Shower Start Finder

The longitudinal granularity and MIP sensitivity of the CALICE AHCAL enables use of topological information to reconstruct the layer of first hard hadronic interaction (FHI) - the shower start. In multi-particle events three dimensional topological information, and thus transverse granularity, will be required to discriminate showers of different incident particles to establish their shower start separately. This high-level shower information can be used to determine the pion interaction length of the CALICE AHCAL engineering prototype and to correct for longitudinal shower leakage.
In the following chapter, we will describe the first implementation and optimization of an algorithm to reconstruct the shower start for the CALICE AHCAL engineering prototype.

3.1 Algorithm

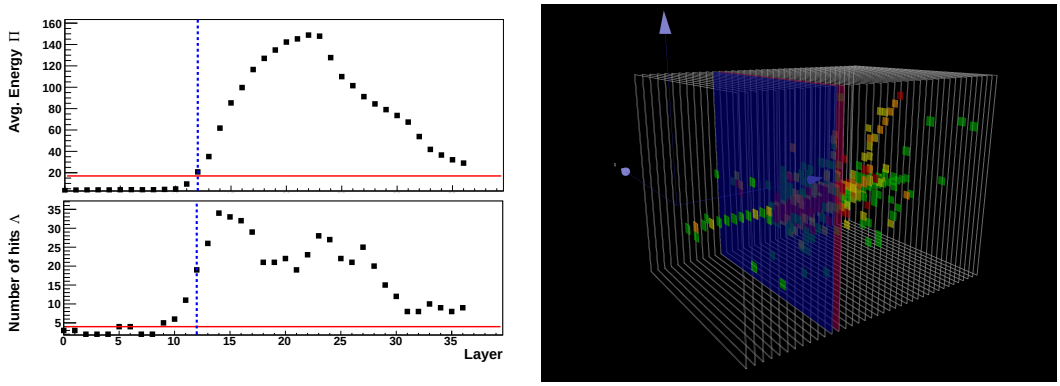

(a) (b)

Figure 14: Visualization of the basic principles of the shower start finder algorithm: (a) The moving window average energy $\Pi = m_i + m_{i+1}$ and the number of hits in two consecutive layers $\Lambda = N_i + N_{i+1}$ with the tuned thresholds indicated by red lines and the reconstructed layer in blue. (b) The event display of the corresponding event with the reconstructed layer in blue and the *true* first hadronic interaction layer in red.

Due to the relatively low hadronic cross section, pions typically produce a MIP track in the detector until they trigger a hadronic cascade. In the layers following the first hard hadronic interaction, we thus expect a sizable increase in the measured energy and number of hits. This is the key insight exploited by the algorithm detailed in [16] and adapted by us for the new AHCAL prototype.
The algorithm is based on a moving window of length w in which the average

measured energy

$$m_i = \frac{\sum_{k=0}^{i} E_k + \sum_{k=0}^{w-i} 1.4\,\mathrm{mip}}{w} \qquad i \leq w$$
$$m_i = \frac{\sum_{k=i-w}^{i} E_k}{w} \qquad i \geq w \tag{11}$$

is calculated. For the first few layers, the moving window extends beyond the detector. For these virtual layers a mip-track with an average energy of 1.4 mip is assumed. The layer of the first hard hadronic interaction is reconstructed to be in layer i if

$$\Pi := m_i + m_{i+1} \geq E_{threshold}$$
$$\text{and} \qquad \Lambda := N_i + N_{i+1} \geq N_{threshold} \tag{12}$$

the sum of both the moving window average of the energy m_i and the number of hits N_i in two consecutive layers exceeds a threshold. These quantities and the corresponding thresholds are visualized in Figure 14. These thresholds can not easily be determined from first principles, because of soft interactions, which also increase the measured energy and number of hits in layers prior to the first hard hadronic interaction. The thresholds $E_{threshold}$ and $N_{threshold}$ will have to be optimized using simulations.
For the previous prototype a window length of $w = 10$ was advantageous to suppress noise effects. Recent developments in SiPM technology however have allowed for a practically noise-free detector. The window size w will be optimized as well. To perform these optimizations an efficiency estimate, which can be maximized, is required.

3.2 True First Hadronic Interaction Layer

For simulated events the *true* first hadronic interaction layer can be obtained, because detailed interaction information is available. To create a sample on which the reconstruction algorithm can be optimized - a sample for which the *true* FHI Layer is known - events with elastic or soft hadronic interactions have to be removed. This is done so that for this optimization sample, the MC first interaction layer coincides with the *true* first hadronic interaction layer. This is necessary as many of the interactions flagged by the simulation as hadronic, are soft leaving the initial hadron with most of its energy. Because a distinction of the initial particle after the interaction and the generated secondary particles is not possible, all of them will be referred to as *secondary*. This indistinguishability

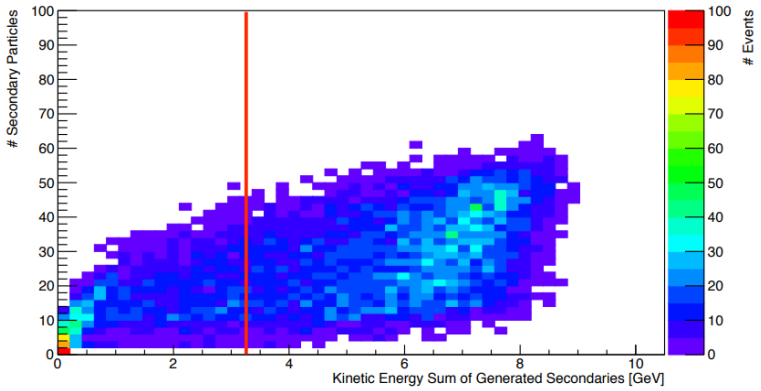

Figure 15: Correlation plot of the number of secondary particles n versus the kinetic energy sum of the generated secondary particles for 10 GeV pions. The red line indicates the implemented cut to reject soft interactions [15].

also creates the need for the first interaction to be a hard hadronic one - later interactions of the initial particle are not easily traceable in the simulation.[1]
The hardness of a hadronic interaction can be classified by the kinetic energy sum of the secondary particles *generated* in the interaction

$$E_{kin}^{\text{gen}} = \sum E_{kin}^{sec} - E_{kin}^{h_{lead}}. \tag{13}$$

$\sum E_{kin}^{sec}$ is the sum of the kinetic energies of all secondary particles. $E_{kin}^{h_{lead}}$ is the kinetic energy of the leading hadron - the hadron with the same type as the initial particle and the highest momentum projected onto the primary hadron's momentum. Subtracting these two quantities thus yields an estimate of the kinetic energy sum of the secondary particles *generated* in the interaction [6].
Figure 15 shows a correlation plot of the number of secondary particles n versus the kinetic energy sum of the generated secondary particles. The high density spot at E_{kin}^{gen}=0 and $n < 5$ corresponds to elastic interactions. Elastic and soft interactions are effectively removed from the optimization sample by rejecting events with E_{kin}^{gen} less than one third of the kinetic energy of the initial hadron, ensuring that the a sizable fraction of its energy went into the generation of secondary particles.
An algorithm optimized on the remaining optimization sample can then be expected to also provide reliable estimates of the position of the first sizable energy release for events with elastic or soft interactions upstream.

[1] For more details, see [6]

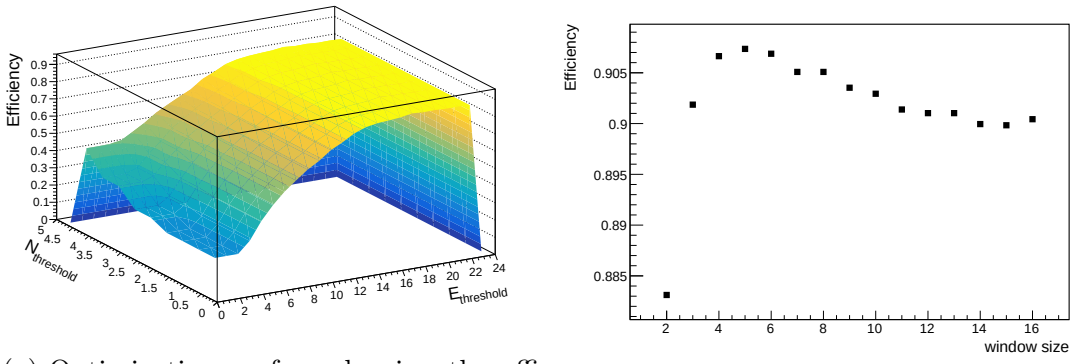

(a) Optimization surface showing the efficiency versus the two thresholds

(b) Efficiency for different window sizes

Figure 16: Threshold and window size optimization on a 10 GeV π^- sample.

3.3 Optimization

With this optimization sample, we can test our reconstruction algorithm and tune the thresholds. To qualify how well the algorithm is performing, an efficiency estimate is required. As it is more important to be close to the *true* layer of first hadronic interaction in a large fraction of all cases than to be exactly right in a smaller fraction, the efficiency is chosen to be the fraction of events reconstructed to have a shower start coinciding with the *true* FYI layer within two layers.
Figure 16 (a) shows the efficiency plotted versus the two thresholds for a 10 GeV π^- sample. For energy thresholds $E_{threshold} \geq 16$ MIP the efficiency plateaus, reaching a maximum at approximately 17 MIP. In this plateau region the hit threshold $N_{threshold}$ does not have an impact on the efficiency of our algorithm. Thus an arbitrary value can be chosen; it is subsequently set to one. To determine the optimal window size w this optimization was performed for window sizes in the range from 2 to 15. Figure 16 (b) shows the efficiency with the optimal thresholds for every window size. The best efficiency is obtained for a window size of five. Figure 17 (a) shows the difference between the *true* and the reconstructed FHI layer for a 10 GeV π^- sample. To ensure statistical independence different samples were used to establish the optimal thresholds and to determine the reconstruction efficiency. For roughly 93% of the events, the reconstructed shower start coincides with the *true* FHI layer within two layers.
It is reasonable to assume the energy threshold $E_{threshold}$ to be dependant on the energy of the initial particle $E_{initial}$. To ensure utility over a wide range of energies, the optimization was repeated for 30 GeV pions.

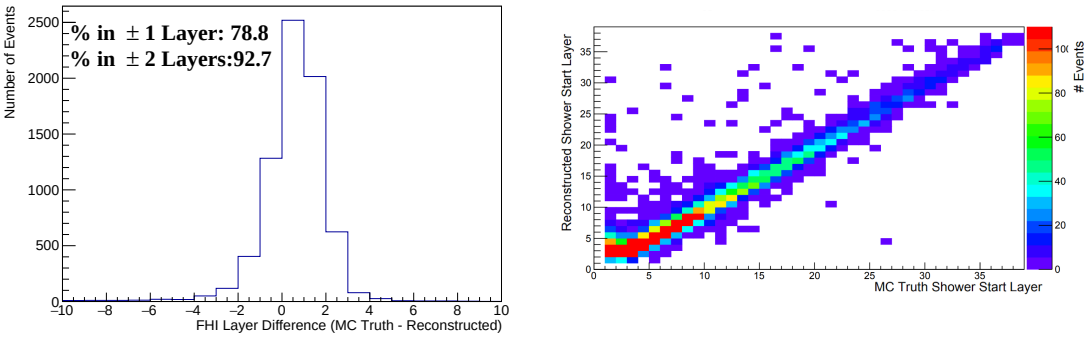

Figure 17: Difference and correlation plot of *true* and reconstructed FHI Layer after optimization for 10 GeV pions.

A second threshold value $E_{threshold}(30\,\text{GeV}) = 25$ MIP was obtained, allowing a linear fit

$$E_{threshold}(E) = 0.4E + 13 \text{ MIP} \qquad \text{with } E \text{ in GeV} \tag{14}$$

to extrapolate threshold values for various beam energies E. Table 3 shows the efficiencies for a sample of energies ranging from 10 to 100 GeV. For energies above 30 GeV the efficiency is well above 95% demonstrating the adequacy of a linear fit to extrapolate to threshold values for higher energies.
Outside of a testbeam environment, shower leakage poses a problem for this approach as the measured energy response of the detector is not a prior a good measure for the energy of the initial particle. Even though the leakage correction developed in this work (See Section 5.2) depends on the shower starting layer, an iterative method is a promising solution: The uncorrected energy measure is used to choose the thresholds to determine the shower start layer, on the basis of which the leakage correction can be applied to the measured energy. This procedure can be repeated until the energy response converges.

	10 GeV	30 GeV	50 GeV	70 GeV	80 GeV	100 GeV
% of events						
equal Layer	26.0	37.5	39.6	41.0	41.8	44.0
within ±1 Layer	73.2	84.0	86.6	87.3	87.0	87.9
within ±2 Layers	92.7	96.5	96.5	97.1	97.2	96.6

Table 3: Reconstruction efficiency after optimization for various energies. The energy threshold for higher energies was obtained by extrapolation with a linear fit.

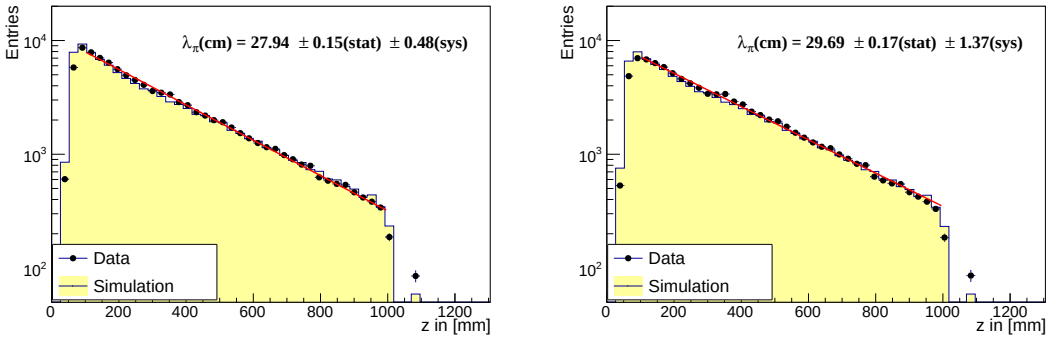

(a) without event selection (b) with event selection

Figure 18: Distribution of the distance of the point of first hard interaction from the calorimeter front face for 10 GeV pions. Data (black dots) and simulation (yellow area) are in excellent agreement. λ_π was determined by fitting Equation 15 to data in the range [100,1000] cm. The systematic error was determined by changing the fit range to [200,900] cm.

4 Pion Interaction Length

With the tuned shower start finder, we can measure the distribution of the first hadronic interaction layer for a large sample of pion showers. As the mean free path for pions is given by the pion interaction length λ_π (See Section 1.1.3), we expect the shower start distribution to follow

$$z_{\mathrm{FHI}} = A_0 \cdot e^{-z/\lambda_\pi}, \tag{15}$$

with A_0 being a normalization constant. Figure 18 and 20 display the shower start distribution for 10 and 30 GeV π^- samples, respectively. The FHI layer was converted into a position in physical space as the position of the corresponding active layer (the centre of the scintillator) - the ensuing uncertainty of the z-position of the reconstructed shower start is represented in the binning of the shown histograms. The event selection (See Section 2.4) employed in (b) was applied to both data and simulation.

For both energies, with and without event selection, simulation and data are in excellent agreement - demonstrating detailed understanding of the detector.

The first two layers in all figures show a deviation from the expected exponential behaviour. This is due to the length of the moving window in which the average energy is calculated (see Section 3.1). Assuming a mip-track in the virtual layers outside of the detector biases the reconstruction algorithm, effectively raising the energy threshold for the first layers. These layers are subsequently excluded from our analysis.

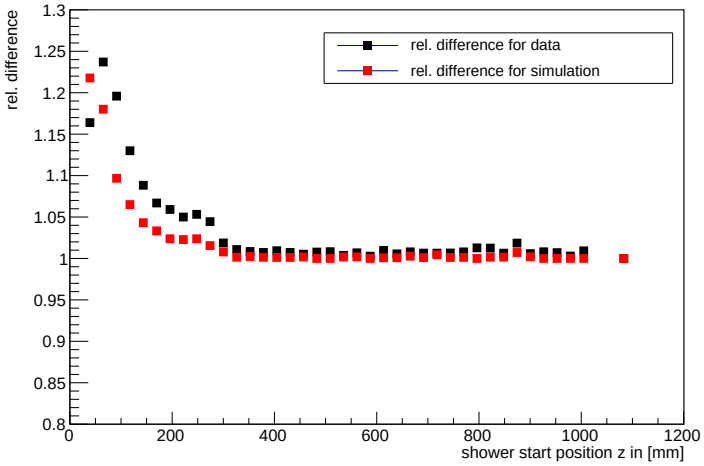

Figure 19: Influence of the event selection on the shower start distribution: the relative difference of the shower start distribution for 10 GeV pions with and without event selection is plotted for each layer.

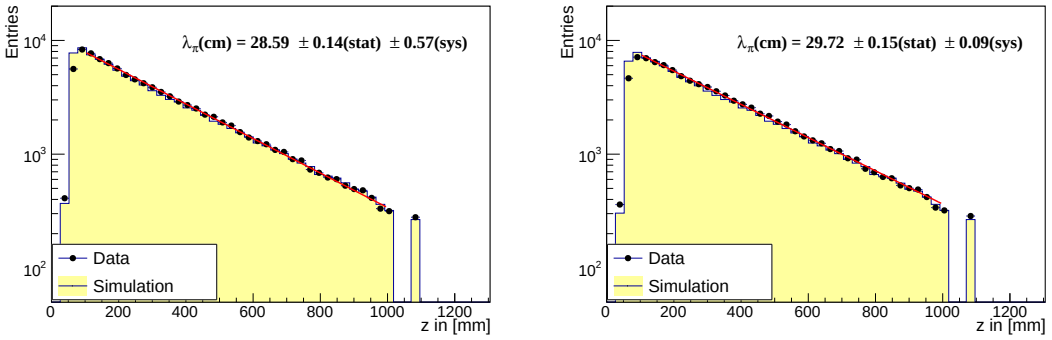

(a) without event selection (b) with event selection

Figure 20: Distribution of the distance of the point of first hard interaction from the calorimeter front face for 30 GeV pions. Data (black dots) and simulation (yellow area) are in excellent agreement. λ_π was determined by fitting Equation 15 to data in the range [100,1000] cm. The systematic error was determined by changing the fit range to [200,900] cm.

Figure 19 shows the relative difference between the shower start distribution with and without event-selection for 10 GeV π^- data (black) and simulation (red). This figure reveals the false-negative rate of our event selection (e.g pions misidentified as electrons) to bias the first ten layers of the shower start distribution by up to 20%. This is due to the fact that early showering pions with an high electromagnetic shower fraction are essentially indistinguishable from electron induced showers. The good agreement between simulation (100% purity) and data suggest no major impurities contaminating this 10 GeV pion sample. It is thus reasonable to use the result obtained without event selection $\lambda_\pi = 27.94 \pm 0.15(\text{stat}) \pm 0.48(\text{sys})$ cm as our estimate for the pion interaction length. The systematic error was determined by varying the fit range. This value is in good agreement with the result of $\lambda_\pi = 27.76$ cm obtained from the material composition of the detector (See Section 2.1).
For 30 GeV pions, a pion interaction length of $\lambda_\pi = 28.59 \pm 0.14(\text{stat}) \pm 0.57(\text{sys})$ cm is found. This slight, but due to the size of the systematic error insignificant, increase of λ_π with energy was seen before in [16].

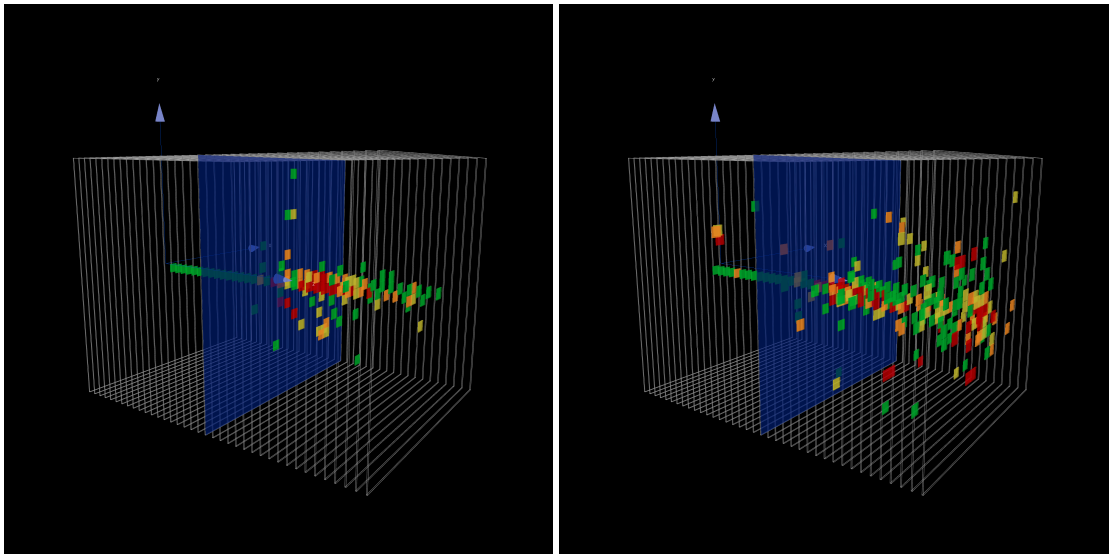

(a) Pion shower with end-fraction 0.005 (b) Pion shower with end-fraction 0.34

Figure 21: Simulated 60 GeV pion showers starting in layer 20 with varying end-fraction.

5 Leakage Correction

The size of the CALICE AHCAL is constrained by the fact that it, as a particle flow calorimeter, has to be located within the magnet solenoid coil of the ILD. The current prototype has an integrated pion interaction depth of 3.6 lambda (See Section 2.1). This makes longitudinal shower leakage - shower particles escaping through the back of the detector - inevitable. Even though leakage in the prototype is considerably larger than it will be for the ILD AHCAL, as it will have 10 additional layers with thicker absorber plates and another lambda in front contributed by the ECAL, leakage will still remain an issue. As an increase in detector length is only possible by enlarging the magnet, this option comes with massive costs. The high granularity of the CALICE AHCAL allows for an intriguing alternative: Use of the topological shower information to correct for longitudinal leakage on an individual particle basis.
A leakage correction based on the shower start and the end-fraction (See Section 5.1) was developed in [19] and is adapted for the new AHCAL prototype in this work.

5.1 Observables sensitive to Leakage

To correct longitudinal shower leakage on an particle by particle basis, we need to identify observables sensitive to it. Figure 22 (a) shows the correlation of the

shower start with the measured energy normalized to the beam energy - the energy of the incident particle. The correlation coefficient $r = -0.6$ quantifies the strong sensitivity of the shower start to longitudinal leakage.
Even though the electromagnetic scale factor (See Section 2.4) was used to connect the measured energy with a physical energy scale, the normalized energy response is only 20% reduced - this is due to the fact that the CALICE AHCAL is almost compensating with $\frac{e}{h} \approx 1.2$. The fraction

$$c_j = \frac{E_{\text{Beam}}}{E_{\text{AHCAL},j}} \tag{16}$$

of the beam energy E_{Beam} (the true shower energy) and the average energy response $E_{\text{AHCAL},j}$ of all showers starting in layer j, yields a correction factor on the basis of the shower start. Figure 22 (b) illustrates this correction factor for a simulated 30 GeV π^- sample. The asymptotic behaviour towards layer 1 corresponds to the hadronic scale factor, which is > 1 because of non-compensation[2]. Towards later layers c_j drastically increases, correcting for longitudinal leakage.
Figure 21 shows two pion showers with the same shower start layer but differing leakage. They are distinct in another variable sensitive to longitudinal shower leakage, the end-fraction. It is defined as

$$ef = \frac{E_{\text{AHCAL},j>34}}{E_{\text{AHCAL,shower}}} \tag{17}$$

the fraction of energy measured in the last four layers of the AHCAL $E_{\text{AHCAL},j>34}$ divided by the entire measured energy $E_{\text{AHCAL,shower}}$ of the shower (e.g. the energy measured in all layers after the shower start). Figure 23 (a) shows the correlation of the end-fraction with longitudinal shower leakage. With a correlation coefficient of -0.72, it is even stronger correlated with leakage than the shower start. Figure 23 (b) shows the corresponding correction factor for simulated 30 GeV pions. For this factor, $E_{\text{AHCAL},j}$ (in Equation 16) corresponds to the average energy response of all showers with an end-fraction j. As the end-fraction is a continuous variable, for this approach to work it has to be binned. A reasonable binning, tested in [19], is given by [0, 0.01, 0.025, 0.05, 0.1, 0.15, 0.2, 0.25, 0.3, 0.35, 0.4, 0.45, 0.5, 0.55, 0.6, 0.65, 0.7, 0.75, 0.8, 0.85, 0.9, 0.95, 1]. The correction factor for the last bin is unreliable as all showers starting in the last four layers are assigned to this bin irrespective of their leakage.

[2]This is no software compensation and only corrects the mean of the energy distribution. It is not able to mend the influence of fluctuations due to non-compensation on the energy resolution.

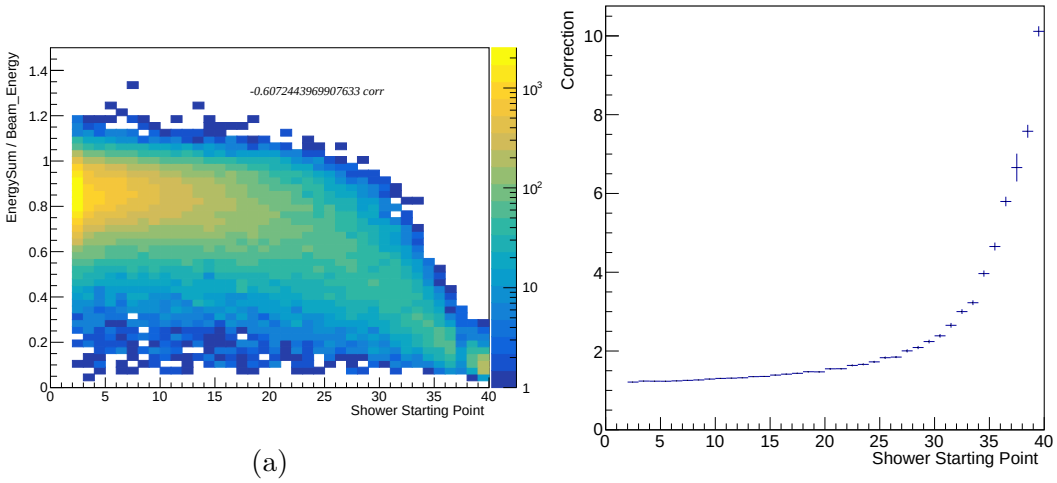

(a) (b)

Figure 22: Correlation of the shower start layer with the fraction of contained energy for simulated 30 GeV pions and the corresponding correction factor as a function of the shower starting point.

Both of these correction factors include the beam energy. To obtain a realistic leakage correction - a correction that only employs calorimeter information and is thus deployable beyond testbeam setups - the measured energy of an event E_{AHCAL} has to be used instead of beam energy information.

5.2 Realistic Leakage Correction

For realistic leakage correction, we have to be able to correct events corresponding to different energies of the incident particle without using beam energy information. To accomplish this, we have to include the measured energy response E_{AHCAL} of the AHCAL. This chapter develops the correction on the basis of simulated events, the application on data is the topic of the next chapter (See Section 5.3). Figure 24 shows a three dimensional plot with the shower start and the end-fraction spanning the x-y plane and the measured energy extending in the z-direction. Events with different energies (different colours) occupy different regions in this 3D space. Even though there is some overlap, this separation - and thus this set of variables - allows for realistic leakage correction.
Figure 25 (a) shows the correlation of the shower start and the end fraction for a simulated 30 GeV π^- sample. As the correlation $r = 0.74$ is not negligible, an independent and sequential correction depending on each variable separately is not possible. Instead a *template* function $f^{-1}_{st,ef}(E_{\mathrm{AHCAL}})$ is found for each *shower classification bin* in Figure 25 (a). These *template* functions basically correspond

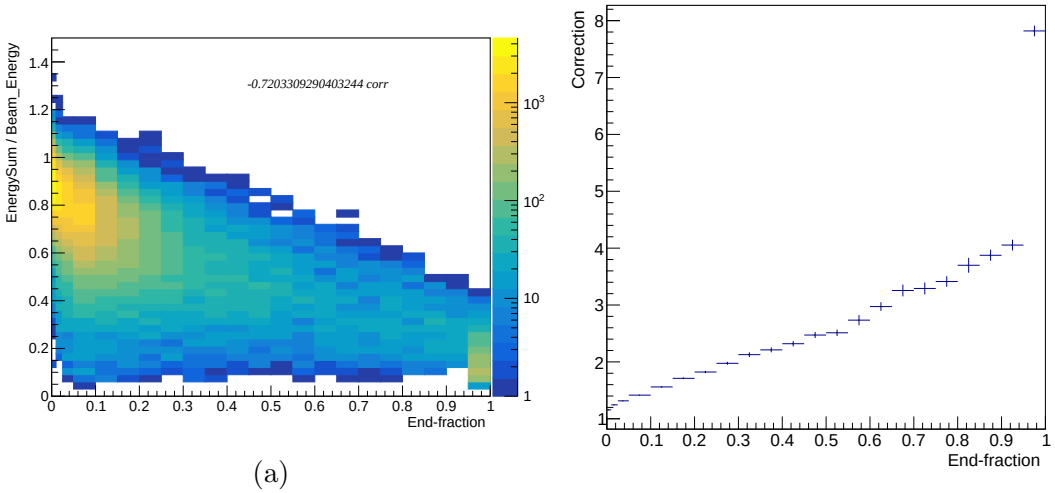

(a) (b)

Figure 23: Correlation of the end-fraction with the fraction of contained energy for simulated 30 GeV pions and the corresponding correction factor as a function of the end-fraction.

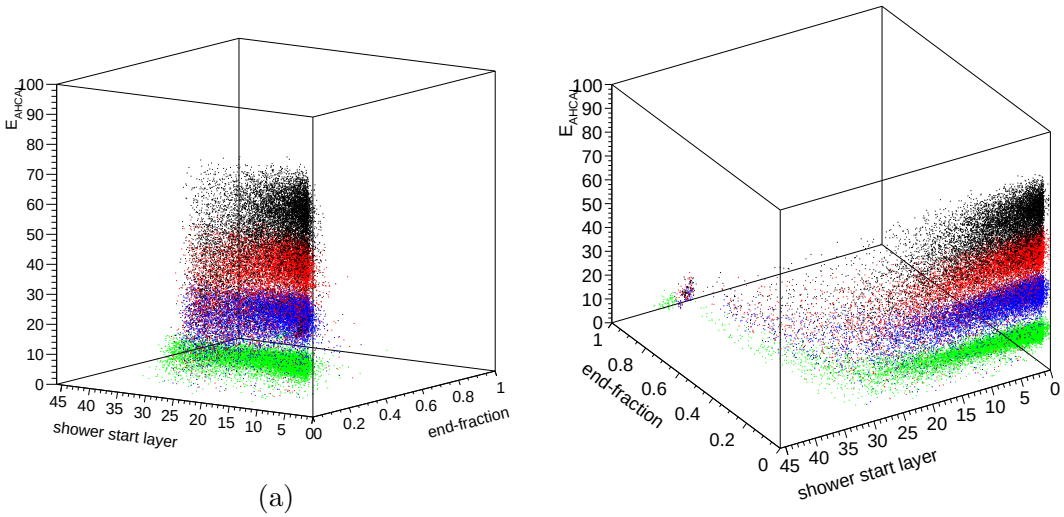

(a) (b)

Figure 24: Samples of different energies (different color) in a 3D space spanned by the shower start, the end-fraction and the measured energy response. Events of different energy tend to occupy distinct regions in space. Despite some overlap, this separation allows for realistic leakage correction.

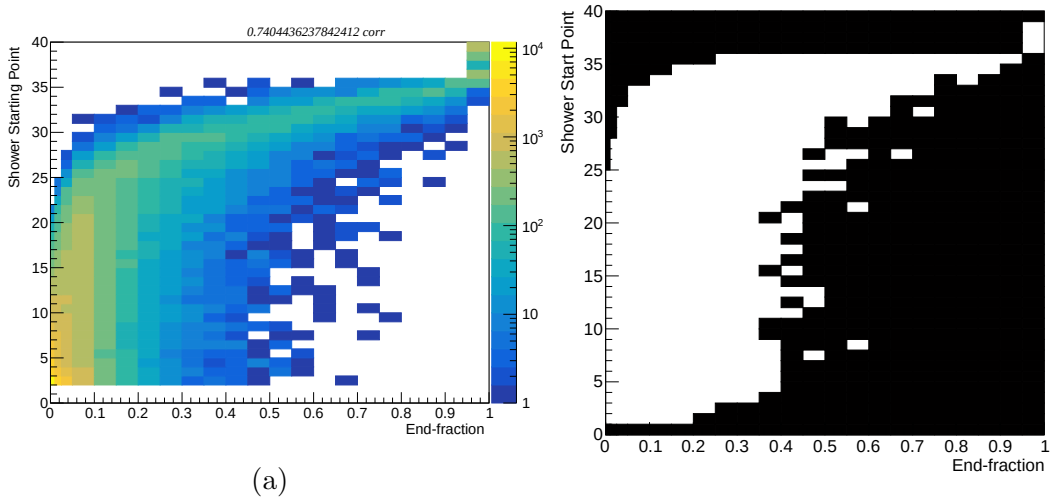

(a) (b)

Figure 25: Correlation of the end-fraction with the shower start for simulated 30 GeV pions. (a) shows the *shower classification bins* for which the *template* function are determined. Each shower is corrected by a functions depending on the bin corresponding to its showers start and end-fraction. (b) shows the bins (white) for which a template function was found in our analysis.

to a 3D *look-up table* of correction factors - with the third dimension E_{AHCAL} being continuous. Figure 26 shows two of these *template* functions; they are obtained by fitting the measured energy E_{AHCAL} as a function of beam energy E_{beam}. (a) is the correction function for the shower start $st = 2$ and end-fraction $ef = 0\%$ bin - an example of a *template* function for showers with practically no leakage, only applying the hadronic scale factor. (b) shows the *template* function for showers starting in layer 26 with an end-fraction of 20%. The measured energy clearly grows sub-linearly with beam energy due to longitudinal leakage. The corresponding *template* function captures this behaviour and corrects for it.

Because the dependence of the measured energy on the beam energy changes depending on leakage, quadratic fits are allowed if they can capture significantly more variance than linear fits. If the quadratic term is very small (< 0.0001), a linear fit is preferred. Figure 25 shows all the bins for which a template function was found (white) in our analysis. For the other bins (black) no template function could be found. This is due to too little showers with these shower variables at different energies in our sample. As a crude estimation of the correction functions for these bins, the *template* function of the nearest white bin was used.

With these template functions a realistic leakage correction is established. For every event the shower start st and the end-fraction ef are determined. Depending on these topologically informed shower variables, the *shower classification bin*

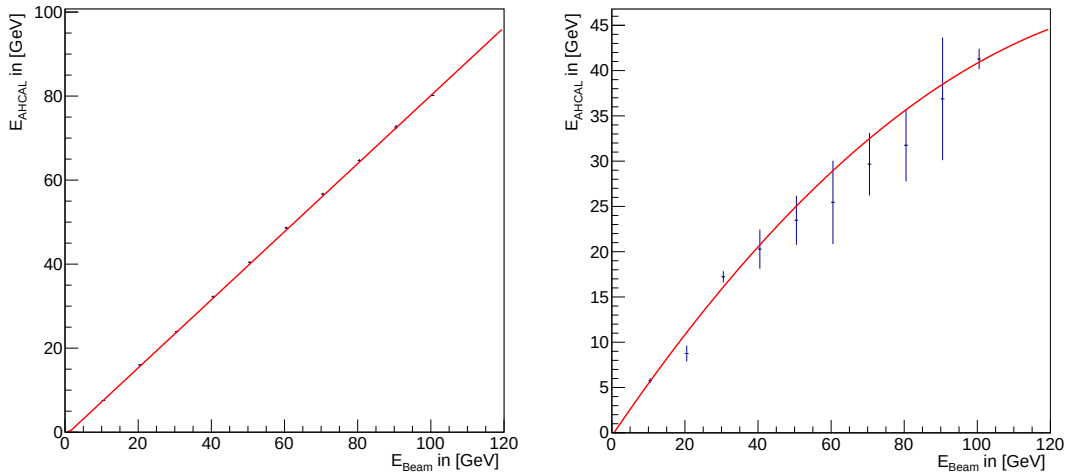

(a) Template function for a $st = 2$ and $ef = 0\%$

(b) Template function for a $st = 26$ and $ef = 20\%$

Figure 26: Template Functions for two different *shower classification bins*. (a) is template function for shower with basically no leakage, only applying the hadronic scale factor. (b) portrays a template function capturing and correcting the sub-linear rise of the energy response due to leakage.

is determined and the corresponding *template* function $f^{-1}_{st,ef}(E_{\mathrm{AHCAL}})$ is applied to the measured energy E_{AHCAL}, yielding the leakage corrected energy estimate. Figure 28 shows the energy spectra for 10 and 100 GeV pions before and after leakage correction. The hadronic scale factor is applied on both the corrected and uncorrected spectra for better comparison. For the uncorrected spectra 10 GeV$/f_{2,0}(10$ GeV) is used as scale factor. As these distributions are highly non-Gaussian, because of their leakage tails towards lower energies, the *root mean squared* RMS cannot be used to establish the energy resolution. Figure 27 shows that a Gaussian with RMS as standard deviation is not able to reproduce non-Gaussian data with a leakage tail. RMS_{90}, the *root mean squared* of the smallest interval containing 90% of the data, has been established as a robust and relatively tail-insensitive measure to quantify the energy resolution [3]. A Gaussian with a standard deviation corresponding to RMS_{90} captures the biggest part of the energy spectrum in Figure 27 adequately. The absolute energy resolution will therefore be identified with the RMS_{90} of the energy spectrum, yielding a conservative estimate of the improvements achieved by the leakage correction. The relative energy resolution corresponds to the RMS_{90} divided by the mean of same interval. With this in mind, Figure 28 reveals our leakage correction to improve the relative energy resolution by roughly 1% for low energies and 41% for high energies. In the case of 100 GeV a drastic reduction of the leakage tail

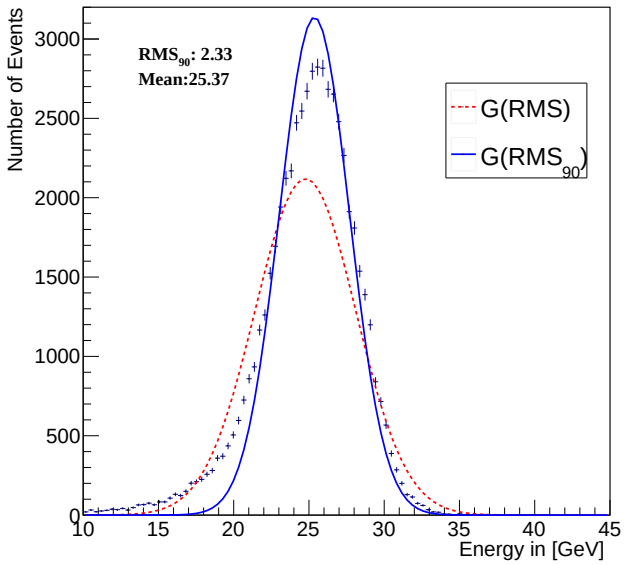

Figure 27: Comparison of RMS and RMS_{90} as standard deviation of a Gaussian fit on a non-Gausian energy spectrum with leakage tail.

is achieved.

Figure 29 shows the energy resolution of the CALICE AHCAL engineering prototype for simulated pion showers of various energies. Red data points show the energy resolution without correction. The energy resolution with the implemented leakage correction corresponds to the blue data points. An estimate of the energy resolution without leakage effects (black data points) is obtained with events showering in the first two layers.

To quantify the reduction of leakage and its influence on the energy resolution, an additional term has to be added to the parametrization of the energy resolution as function of the beam energy (Equation 8). The parameters a,b and c are detector specific. To avoid them accounting for variance caused by leakage, they are determined with the "leakage-free" sample, by fitting the black data points up to 60 GeV - avoiding higher energies and the remaining influence of leakage despite of the applied cut. Due to lack of data points on the sharp rise of the energy resolution, a distinction of $a/\sqrt{E}$ and b/E is not possible. As b accounts for noise and is known to be very small, it is neglected to avoid over-fitting.

On the basis of the "leakage-free" sample $a = 41.7\%$ and $c = 3.0\%$ are obtained. With these parameters fixed, a leakage term of the form

$$\frac{rms_{90}}{\mu} = \frac{a}{\sqrt{E}} \oplus c \oplus d \cdot E^{1/4} \qquad \text{with } E \text{ in GeV} \tag{18}$$

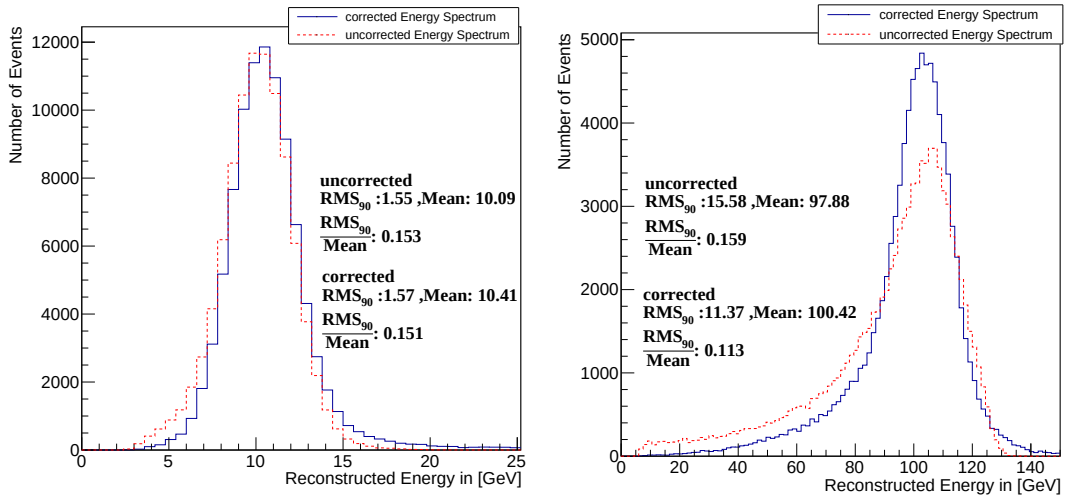

(a) 10 GeV pions (b) 100 GeV pions

Figure 28: Comparison of corrected and uncorrected energy spectra for simulated 10 and 100 GeV pions. The implemented leakage correction can drastically improve the energy resolution for high energies (41%) by reducing the leakage tail.

is found to fit all three samples. The implemented leakage correction is able to cut this leakage term $d_{\text{uncorrected}} = 22.4 \cdot 10^{-2}\%$ in half $d_{\text{corrected}} = 10.3 \cdot 10^{-2}\%$. With this reduction of leakage an by up to 41% improved energy resolution is achieved.

5.3 Application to Data

The following chapter is a preliminary study of the implemented longitudinal leakage correction applied to data. Due to time constraints on this work, no proper event selection for the relevant energy range could be developed. The data is thus taken at face value without verification of the purity of the samples. Figure 31 (a) shows the energy resolution as a function of beam energy for the naive approach of applying the *template* functions determined for simulated pion showers on data. These correction functions only yield a moderate improvement for high energies, while degrading the energy resolution for low energies. This is most likely due to small differences of simulated and real pion showers, resulting in showers with equivalent leakage ending up in different *shower classification bins*. One reason for this discrepancy are small differences in the longitudinal shower profiles for simulation and data. Another difference is the electromagnetic scale factor (See Section 2.2), which in this work was determined with simulated electrons. Application of this factor on data most likely yields an energy result that

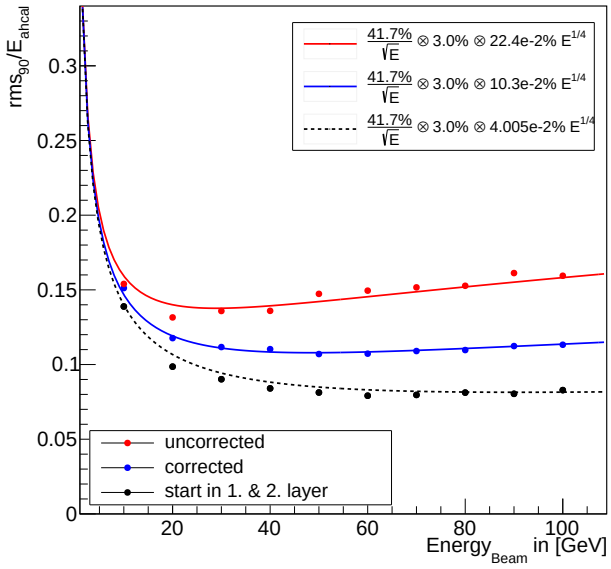

Figure 29: Un-/corrected and "leakage free" energy resolution for simulated pion showers as a function of beam energy. The stochastic and constant term are determined on the basis of the "leakage free" sample.

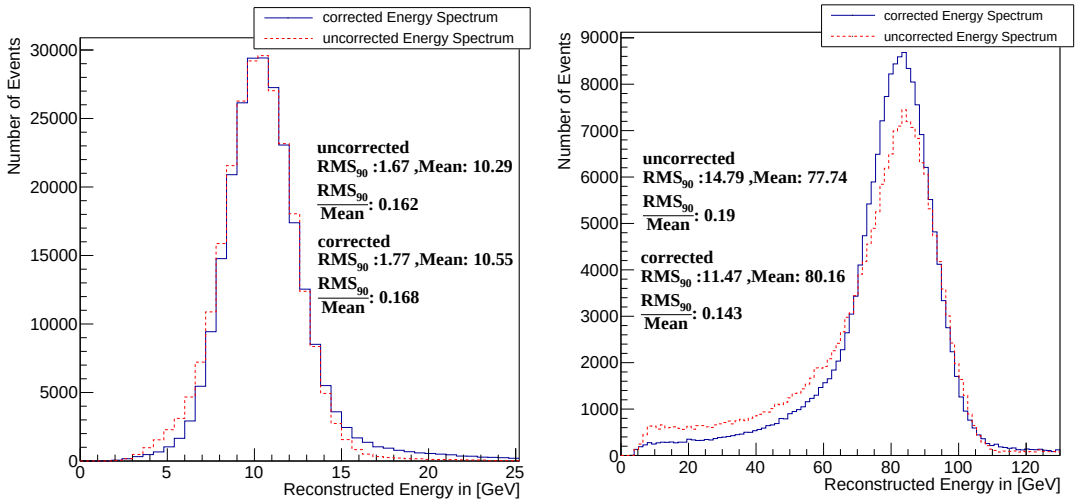

(a) 10 GeV pions (b) 80 GeV pions

Figure 30: Comparison of corrected and uncorrected energy spectra for 10 and 80 GeV pions. The implemented leakage correction can improve the energy resolution for high energies (33%) by reducing the leakage tail.

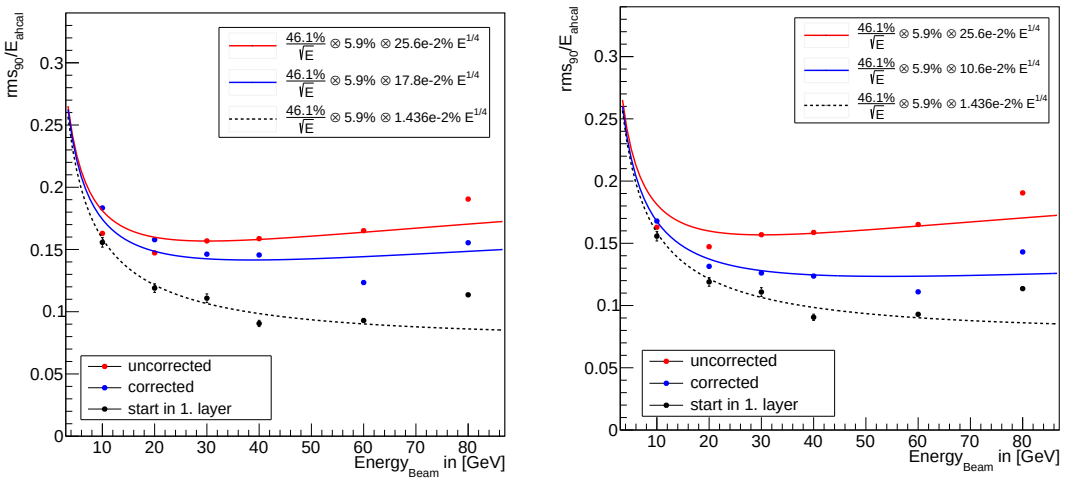

(a) Correction with *template* functions obtained for simulation

(b) Correction with *template* functions obtained for data

Figure 31: Un-/corrected and "leakage free" energy resolution for pion showers as a function of beam energy.

slightly deviates from that of equivalent simulated showers - as there probably is a slight discrepancy between the electromagnetic scale factor for simulation and data [6].

To avoid miss-classification due to small differences between simulated and real showers, *template* functions for data were determined by repeating the process described for simulated shower (See Section 5.2). Figure 30 shows the comparison of uncorrected and corrected energy spectra for 10 and 80 GeV. For low energies the correction recovers a more Gaussian energy distribution at the cost of a slightly reduced energy resolution. For 80 GeV the leakage tail is reduced, improving the energy resolution by 33%.

Figure 31 (b) shows the energy resolution for uncorrected, corrected and "leakage-free" showers as a function of the beam energy. The "leakage-free" sample is obtained as described in Section 5.2. The remaining influence of leakage in spite of the applied cut is clearly visible for higher energies. The procedure to determine a parametrization for the energy resolution is repeated. The stochastic and the constant term are determined on the basis of the "leakage free" sample with energies up to 40 GeV - avoiding the sizable remaining influence of leakage for higher energies.

The stochastic term a is found to be 46.1%, the constant term c to be 5.9%. With these values fixed the parametrization including a leakage term (Equation 8) is fitted to all three samples. As for simulated shower, the leakage correc-

tion is able to cut the leakage term $d_{uncorrected} = 25.6 \cdot 10^{-2}\%$ more than in half $d_{corrected} = 10.6 \cdot 10^{-2}\%$. This implementation of a realistic leakage correction improves the energy resolution for data by up to 33%.

	simulation	data		simulation	data
			RMS_{90}/μ at 10 GeV		
stochastic term a	41.7%	46.1%	uncorrected	0.153	0.162
constant term c	3.0%	5.9%	corrected	0.151	0.168
			ratio	1.013	0,964
leakage term			at 80 GeV		
"leakage-free" d	$4.0 \cdot 10^{-2}\%$	$1.4 \cdot 10^{-2}\%$	uncorrected	0.151	0.19
uncorrected $d_{uncorrected}$	$22.4 \cdot 10^{-2}\%$	$25.5 \cdot 10^{-2}\%$	corrected	0.11	0.143
corrected $d_{corrected}$	$10.3 \cdot 10^{-2}\%$	$10.6 \cdot 10^{-2}\%$	ratio	1.37	1.33

Table 4: Comparison of the energy resolution parameters and the impact of the implemented leakage correction for simulation and data.

Table 4 shows a comparison of the results for simulation and data. The results for data are only preliminary as no event selection was applied and the sample purity has not been verified. For 10 GeV shower the energy resolution does not improve, for data it increases by 4%. The implemented leakage correction is able to cut the uncorrected leakage term $d_{unccorrected}$ in half for both simulation and data. This leads to an improvement of the energy resolution for 80 GeV pion showers by 37% and 33% in simulation and data, respectively. These results show the implemented leakage correction to be functioning for both simulation and data. A study quantifying the impact of the leakage correction on pure data samples will have to be performed.

Summary

Future e^+e^- colliders require an unprecedented jet energy resolutions of 3-4% over a wide range of energies. This can most likely not be achieved with classical calorimetry. One concept rising to the challenge is the particle flow approach. It aims to reconstruct every jet particle in the detector individually, to then use the measurement of the best suited sub-detector for each particle type. For this approach to work, tracks in the tracking system have to be matched with showers in the calorimeter system. This complex pattern recognition problem is only solvable with topological shower information. To obtain topological information, the calorimeter has to be highly granular. One concept of such a highly granular calorimeter is the ILD AHCAL.

This work studied topological shower reconstruction in the CALICE AHCAL engineering prototype. An algorithm to find the layer of the first hard hadronic interaction - the shower start - was implemented and optimized. This shower start finder exploits the sharp rise in energy measured in the layers subsequent to the layer of the first hadronic interaction. It was optimized with simulated showers for which the true shower start is known and reconstructs the shower start for 10 GeV pions within two layers with an efficiency of 93%. For energies of 30 GeV or above the efficiency is larger than 95%.

This high level shower information was used to measure the pion interaction length as a cross-check for the detector material composition. The pion interaction length was measured to be $\lambda_\pi = 27.94 \pm 0.15(\text{stat}) \pm 0.48(\text{sys})$ cm. This value is in excellent agreement with the result of $\lambda_\pi = 27.76$ cm obtained from material composition.

Topological shower information can also be used for leakage correction. This is especially relevant because the ILD AHCAL is spatially constraint, as it is a particle flow calorimeter, which has to be located within the magnet solenoid coil. Thus an increase in detector size comes with massive costs.

The shower start layer together with the end-fraction, the fraction of the shower energy deposited in the last four layers of the detector, are two topological observables which can be used for longitudinal leakage correction. Due to their high correlation an independent and sequential correction depending on each variable separately is not possible. Instead *template* functions $f^{-1}_{st,ef}(E_{AHCAL})$ are found for each pair of these topological observables, correcting the measured shower energy E_{AHCAL} on the basis of topological information. Because of slight differences in simulated and measured pion showers, different sets of *template* functions had to be determined for simulation and data.

This work showed that these *template* functions allow a realistic leakage correction - one based only on calorimeter information. It improves the simulated energy resolution for pion showers in the energy range of 10 to 100 GeV by up to 41%. The performed application of the correction on data was only preliminary as no validation of the sample purity could be performed. Nonetheless, it was able to show the implemented leakage correction to be promising, achieving an energy resolution improved by up to 33%.
In future studies of topological shower reconstruction, it might be worthwhile to employ deep learning methods. Both the reconstruction of the shower start layer, as well as the classification of showers to subsequently correct for leakage, are tasks common to those for which deep learning showed to excel in the recent past. These methods allow to identify and utilize additional relevant observables to perform the classification task in a higher dimensional space. Thus possibly allowing to improve both the shower start reconstruction efficiency and the energy resolution beyond what was possible in the scope of this work.

References

[1] M. Thomson, "Modern particle physics," Cambridge University Press, 2013

[2] M. Tanabashi *et al.* [Particle Data Group], "Review of Particle Physics," Phys. Rev. D **9**8 (2018) no.3, 030001. doi:10.1103/PhysRevD.98.030001

[3] M. A. Thomson, "Particle Flow Calorimetry and the PandoraPFA Algorithm," Nucl. Instrum. Meth. A **6**11 (2009) 25 doi:10.1016/j.nima.2009.09.009 [arXiv:0907.3577 [physics.ins-det]].

[4] F. Sefkow, A. White, K. Kawagoe, R. Pschl and J. Repond, "Experimental Tests of Particle Flow Calorimetry," Rev. Mod. Phys. **8**8 (2016) 015003 doi:10.1103/RevModPhys.88.015003 [arXiv:1507.05893 [physics.ins-det]].

[5] MissMJ *Standard Model of Elementary Particles*. Licensed under CC BY 3.0. URL: https://commons.wikimedia.org/wiki/-File:Standard_Model_of_Elementary_Particles.svg

[6] O. Hartbrich, "Scintillator Calorimeters for a Future Linear Collider Experiment," doi:10.3204/PUBDB-2016-02800

[7] R. Wigmans, "Calorimetry, Energy Measurements in Particle Physics," Oxford Science Publications, Oxford University Press, 2000

[8] S. Agostinelli *e*t al. [GEANT4 Collaboration], "GEANT4: A Simulation toolkit," Nucl. Instrum. Meth. A **5**06 (2003) 250. doi:10.1016/S0168-9002(03)01368-8

[9] N. Feege, "Low-energetic hadron interactions in a highly granular calorimeter," DESY-THESIS-2011-048.

[10] I. C. Brock, "Physics at the terascale,"

[11] E. Brianne, "Time development of hadronic showers in a Highly Granular Analog Hadron Calorimeter," doi:10.3204/PUBDB-2018-02769

[12] H. Kolanoski and N. Wermes, "Teilchendetektoren : Grundlagen und Anwendungen," doi:10.1007/978-3-662-45350-6

[13] T. Behnke *e*t al., "The International Linear Collider Technical Design Report - Volume 4: Detectors," arXiv:1306.6329 [physics.ins-det].

[14] F. Sefkow *et* al. [CALICE Collaboration], "A highly granular SiPM-on-tile calorimeter prototype," J. Phys. Conf. Ser. **1**162 (2019) no.1, 012012 doi:10.1088/1742-6596/1162/1/012012 [arXiv:1808.09281 [physics.ins-det]].

[15] D. Heuchel, Pedestals and MIP Constants, CALICE Collaboration Meeting at Shanghai, 2018, https://agenda.linearcollider.org/event/7799/

[16] B. Bilki *et* al. [CALICE Collaboration], "Pion and proton showers in the CALICE scintillator-steel analogue hadron calorimeter," JINST **1**0 (2015) no.04, P04014 doi:10.1088/1748-0221/10/04/P04014 [arXiv:1412.2653 [physics.ins-det]].

[17] C. Adloff *et* al. [CALICE Collaboration], "Construction and Commissioning of the CALICE Analog Hadron Calorimeter Prototype," JINST **5** (2010) P05004 doi:10.1088/1748-0221/5/05/P05004 [arXiv:1003.2662 [physics.ins-det]].

[18] V. Bocharnikov, Particle Identification in the 2018 AHCAL test beam data, CALICE Collaboration Meeting at Utrecht, 2019, https://agenda.linearcollider.org/event/8109/

[19] CALICE Collaboration [CALICE Collaboration], "Shower Leakage in a Highly Granular Calorimeter," CALICE Analysis Note CAN-029, CALICE-CAN-2011-009.

Erklärung

Ich versichere, dass ich diese Arbeit selbstständig verfasst und keine anderen als die angegebenen Quellen und Hilfsmittel benutzt habe.
Heidelberg, den 20.08.2019,

Unterschrift: _____

Jonas M. Mikhaeil